J. Fluid Mech. (1977), *vol.* 82, *part* 1, *pp.* 53–95
Printed in Great Britain

Turbulent mixing of passive and chemically reacting species in a low-speed shear layer

By R. G. BATT

Engineering Sciences Laboratory, TRW Space and Defense Systems Group,
Redondo Beach, California 90278

(Received 3 September 1976 and in revised form 6 January 1977)

A series of experiments has been conducted in a low-speed wind tunnel in which measurements were performed in a two-dimensional turbulent shear layer experiencing the mixing of both a passive and a chemically reacting species. The low-temperature air in the jet's primary flow was seeded with dilute concentrations of N_2O_4 so that the dissociation reaction $N_2 + N_2O_4 \leftrightarrow 2NO_2 + N_2$ occurred in a near-equilibrium manner within the mixing layer owing to the turbulent mixing properties and the imposed temperature gradient. Mean and fluctuating values of velocity, temperature and NO_2 concentration were measured up to axial distances of 25 in. for jet velocities of 23 and 50 ft/s ($Re_x \leqslant 7 \times 10^5$) and for three primary temperatures (252, 273 and 305 °K). Velocity and temperature measurements were performed with hot-wire probes, whereas a fibre optics light sensor probe was used to measure NO_2 concentrations. Local correlations between species and other fluid properties were obtained by positioning a hot-wire sensor within the light gap of the fibre optics probe and simultaneously recording output signals from both probes. A relatively complete set of turbulent statistics was measured for the non-reacting shear layer, including such results as temperature/species correlations, probability densities, filtered and unfiltered moving-frame velocities, skewness and flatness factors, spectra, velocity and temperature integral scales, intermittency factors for velocity, temperature and passive species, and conventional intensities. Some typical results from the investigation are as follows: the turbulent Schmidt and Lewis numbers were 0·5 and 1·0 respectively; the correlation between passive NO_2 concentration and temperature was approximately 0·95; dramatic changes consistent with equilibrium chemistry occurred in NO_2 concentration profiles with chemical reaction; velocity, temperature and concentration spectra were comparable over a $2\frac{1}{2}$-decade range in wavenumber (k^{-2}); spectra, probability densities, time-trace data and smoke-seeded shear-layer photographs indicate that, for axial locations $x = x_0 \geqslant 18{\cdot}5$ in. and for speeds $u_1 \geqslant 23$ ft/s, undisturbed edge fluid rarely penetrates completely across the mixing region. Although not specifically addressed during the current study, measured results herein suggest that the turbulent motion for the present shear layer is characterized more by random and/or three-dimensionality effects than by large-scale two-dimensional coherent structures, as has been observed recently in other shear-layer investigations.

1. Introduction

In obtaining theoretical solutions for turbulent flows, phenomenological hypotheses are often used in order to relate fluctuating quantities to mean flow properties. The familiar eddy-viscosity and eddy-diffusivity coefficients are typical of this approach and reasonable agreement between mean profile prediction and measurement is obtained for non-reacting flows. The situation, however, is not as satisfying in the case of chemically reacting turbulent flows. Investigations dealing with reacting turbulent wakes behind hypersonic bodies (which provided the original motivation behind the current study), supersonic combustion, chemical lasers, nuclear fireballs, chemical-reactor design and industrial exhaust plumes all involve questions fundamental to the chemical kinetics in a turbulent flow field. Not only does there exist uncertainty as to the effect of turbulence on the chemistry and vice versa but also related questions of flow homogeneity, suitable reaction-rate approximations, primary transport mechanisms, passive-species mixing characteristics, the relative magnitude of temperature/species correlations and appropriate mixing models still remain unresolved.

Analytical methods for calculating reacting turbulent flows are concerned both with mean flow quantities as well as with such statistical properties as fluctuating intensities, power spectral density and turbulence scales. In addition to the turbulent-flame theories of Bush, Feldman & Fendell (1976), Bilger (1976), Spalding (1976) and Donaldson & Varma (1976) and the many specialized analyses directed primarily at the hypersonic-wake problem (Lees & Hromas 1962; Webb & Hromas 1965; Lin & Hayes 1964; Sutton & Camac 1968; Libby 1976; Proudian & Feldman 1965; Sutton 1968; Lin 1966; Mayer & Divoky 1966), the statistical theories of Torr (1962), O'Brien (1971), Alber & Batt (1976) and Chung (1970) have been developed for turbulent flows in general. Of common concern to the hypersonic-wake investigators was the relative importance of the two transport mechanisms of bulk convection and gradient diffusion, which mix the inviscid external flow with the viscous core of the hypersonic turbulent wake. Since the degree of mixing directly affects the rate at which chemical reactions occur, the choice of mixing process influences significantly the calculated results for non-equilibrium turbulent flows. Typical of this dependence is the method of solution for the species conservation equation in the homogeneous mixing model (Lees & Hromas 1962), which uses the quasi-steady or laminar approximation for the chemical production terms. This formulation for the species source term involves the assumption of an effective reaction-rate expression based on mean flow quantities. Only limited experimental evidence is available with which to determine the degree of applicability of such an approximation. In a similar manner many other details of the flow field, such as the effect of the fluctuating flow properties and correlated fluctuations on the reactant concentrations, as well as the significance of coherent large-scale structures in turbulent shear flows (Brown & Roshko 1974; Moore & Saffman 1975; Roshko 1976), still require experimental study in order to clarify their role in formulating solutions for reacting turbulent flows.

The purpose, therefore, of the present experimental study has been to investigate the turbulent structure and diffusive characteristics associated with the mixing of both a passive and a reacting species in a turbulent shear flow. A substantial amount of shear-flow data, mostly non-reacting but some turbulent chemical kinetics data for

a dissociation reaction in chemical equilibrium, has been generated. While some of the current results duplicate measured data of other investigators, a major portion of the data which follows is considered unique and of interest to those workers developing analyses and/or turbulent mixing models for treating both the scalar mixing problem and the interplay between turbulence and chemistry.

The shear flow chosen for the investigation was a two-dimensional turbulent shear layer. This type of free turbulence not only provides a turbulent structure which is self-preserving and whose property profiles are similar but also includes the two transport mechanisms of bulk convection and gradient diffusion as well as the entrainment (engulfment) features of the intermittent turbulent front. Since the experiments were performed with only dilute species concentrations, the effects of the chemistry on the turbulence were negligible and therefore such non-reacting shear-layer results as those provided by Liepmann & Laufer (1947), Wygnanski & Fiedler (1969), Sunyach & Mathieu (1969; see also Sunyach 1971), Spencer & Jones (1971) and Davies, Fisher & Barratt (1963) have been useful in helping to define the required turbulence data base. Because of several experimentally beneficial chemical properties, the nitrogen tetroxide dissociation reaction

$$N_2 + N_2O_4 \leftrightarrow 2NO_2 + N_2$$

was selected for the current study. This reaction was also used successfully by Wegener (1959) to demonstrate the feasibility of measuring recombination-rate constants in a supersonic nozzle flow.

Although some of the results discussed herein have already been presented by Batt, Kubota & Laufer (1970) and Alber & Batt (1976), the current documentation, representing a summary of experimental results obtained over several years of research, constitutes the initial publication of the major portion of the data which follow. It should also be noted that in the paper by Alber & Batt (1976) the senior author presents an evaluation and review of the implications of the present data base relative to developing both the turbulence model equations and an equilibrium-chemistry model, based on the probability density function (pdf) approach, for treating the chemically reacting low-speed shear layer.

2. Experimental techniques

The turbulent mixing layer (figure 1) investigated herein was established within the test section of the low-speed wind tunnel† shown schematically in figure 2. The tunnel is a vertically oriented recirculating facility with maximum velocities of up to 80 ft/s at the test-section inlet (5 × 24 in.). In order to minimize the buoyancy effects accompanying imposed thermal gradients, the flow is directed vertically downwards through the 5 ft long test section. Four turbulence damping screens and an aluminium honeycomb section are positioned just upstream of the tunnel's stagnation chamber. A tunnel contraction ratio of 8:1 further reduces turbulence intensities such that for the plane mixing-layer configuration the intensity in the core flow is less than 0·4 % whereas for a closed test-section configuration the intensity is less than 0·2 %.

† This tunnel is a modified version of the facility originally constructed by the National Engineering and Science Company (NESCO) to carry out experiments similar to those described herein.

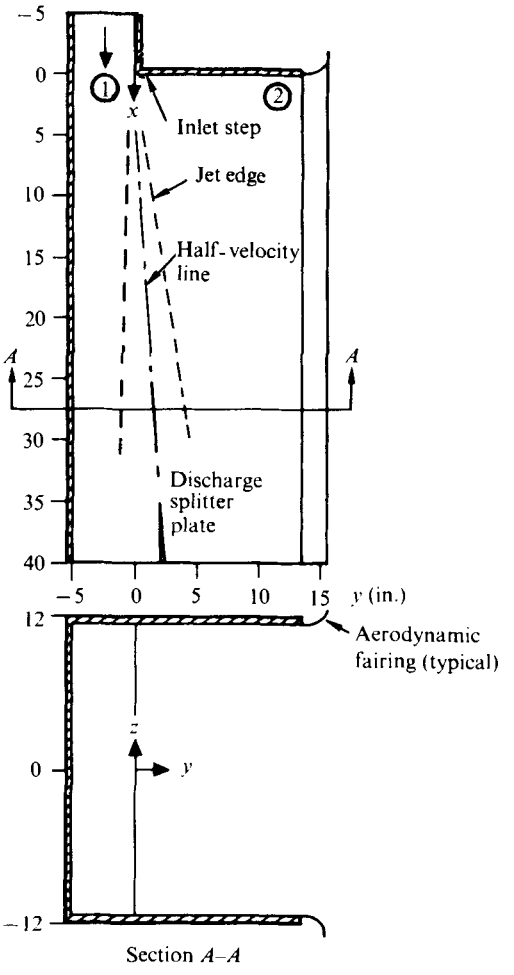

FIGURE 1. Schematic diagram of shear-layer test section.

In the investigation discussed by Batt (1975), shear-layer measurements were performed in the present facility for both a tripped and an untripped mixing-layer configuration. These data showed that disturbing the initial boundary layer with a wire trip caused the shear layer to grow faster ($\sigma = 9$) than the undisturbed mixing region ($\sigma = 12$). The tripped shear layer also exhibited initially an axial enhancement with an overshoot (rather than decay) in peak intensity, as similarly observed by Castro & Bradshaw (1976) for the curved mixing layer. Since these results also indicated that the axial distance x required for the shear layer to achieve its classical asymptotic behaviour was shorter for the untripped case than for the tripped configuration, all measurements in the current investigation were performed with undisturbed initial conditions corresponding to a laminar core-flow boundary layer (figure 3). Also, all measurements described herein were obtained at stations sufficiently far downstream from the mixing-region origin that the jet's turbulence structure was fully developed and self-preserving.

For the reacting shear-layer experiments (§4) the chemical reaction investigated was the decomposition of nitrogen tetroxide (N_2O_4) to give nitrogen dioxide gas (NO_2):

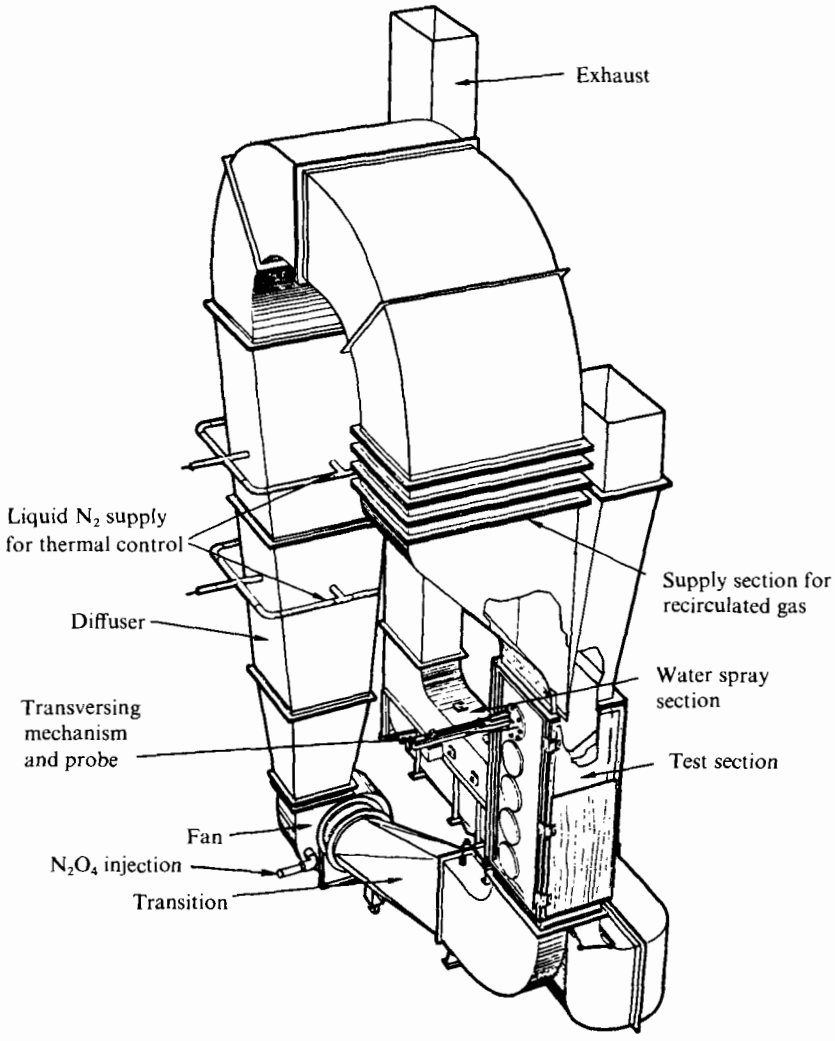

FIGURE 2. Schematic diagram of low-speed wind tunnel.

$N_2O_4 + N_2 \leftrightarrow 2NO_2 + N_2$. By seeding the cold carrier gas (dry air at $-20\,°C$) on the primary side of the mixing region with dilute concentrations of N_2O_4, dissociation of N_2O_4 occurred within the jet owing to the mixing of tetroxide 'rich', cold eddies with clear, 'hot' ambient air eddies. A unique feature of the tetroxide dissociation is that if the temperature is varied from $-20\,°C$ to room temperature the degree of dissociation changes from 0·3 to 0·96. At room temperature, in fact, the dissociation is essentially complete and experiments run with primary and secondary streams at such temperatures thus correspond to the turbulent motion of a passive species (NO_2). Measurements of the mean flow field, fluctuating flow properties and correlated fluctuations were performed at several stations within the jet for core-flow velocities of $u_1 = 23$ and 50 ft/s and temperature ratios of $T_1/T_2 = 0{\cdot}985$, 0·880 and 0·820. Hot-wire probes were used to measure the velocity and temperature data, whereas mean and fluctuating concentration measurements of NO_2 were obtained through use of

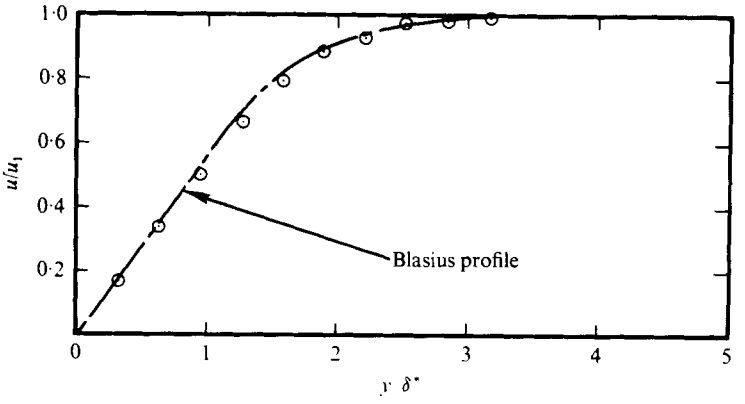

FIGURE 3. Velocity profile for inlet boundary (u_1 = 50 ft/s, δ^* = 0·032 in., x = 2·2 in.).

a fibre optics light sensor probe. Local correlations between passive-species and other fluid properties have also been measured, by positioning a hot-wire sensor within the light gap of the fibre optics probe and simultaneously recording output signals from both probes.

Attached to the wind tunnel's test-section outlet is a stainless-steel cleansing and exhaust system to remove excess contaminants and balance the mass flow between the primary- and secondary-flow sides of the jet. Because of the corrosive nature of nitrogen dioxide gas, a stainless-steel blower was used and the tunnel proper was constructed from aluminium sheeting, which is moderately resistant to the oxidation of NO_2. The thermal control system, which can cool the primary core flow to $T = -20\,^{\circ}\mathrm{C}$ by means of liquid-nitrogen injection, and a reactant control system to feed and regulate the flow of nitrogen tetroxide into the tunnel's primary loop are also shown in figure 2. The N_2O_4 storage (10 lb liquid N_2O_4) and delivery (0·5 lb/min) capability for the reactant control system permits test runs of the order of 20 min for a core concentration level of $[N_2O_4]_a/[N_2] = 0{\cdot}005$. While exposing the secondary-flow side of the half-jet to dry air supplied by a Cargoaire dehumidifier (HC-150), protection of testing personnel in the vicinity of the tunnel from the reactant contamination was successfully accomplished by the tunnel's exhaust system.

Because of the recent interest of investigators in photographing the two-dimensional shear layer, attempts were made during the current investigation to obtain similar optical 'data'. The spanwise photographs (x, y plane) in figure 4 (plate 1) and the motion-picture film clip (64 frames/s) shown in figure 5 (plate 2) were obtained by seeding the primary-flow loop of the wind tunnel with mineral-oil smoke from a Kinney Engineering smoke generator. A high intensity light source was mounted above the jet's inlet step and provided light through a $\frac{1}{4}$ in. lateral light slit aligned in the y direction. Although the pulsed electronic flash unit provided sufficient light intensity to obtain still photographs of the shear layer, even under highly dilute conditions associated with the highest speed investigated (u_1 = 47 ft/s), it was not possible with the available continuous-beam light source and smoke supply system to obtain similar motion pictures for any speeds higher than u_1 = 11 ft/s. Since such sequential photographs illustrate some of the features associated with the shear-layer eddy formation and initial development process (e.g. the vortex pairing process; Winant & Browand

1974) they are included here even though they correspond to a Reynolds number lower than that corresponding to the bulk of the measurements presented herein. Note that the still photographs shown in figure 4 suggest that the orderly large-scale eddy structures (Brown & Roshko 1974), evident at low Reynolds numbers ($u_1 = 11$ ft/s), attenuate with increasing axial distance and increasing Reynolds number. Such an illustration of the behaviour of large-scale coherent eddies, however, should not in itself be considered conclusive since the 'data' in figure 4 represent a limited 'measurement' sample. In a discussion of some of the statistical results which follow, the relative importance of orderly eddy structures will again be evaluated but from the standpoint of measured shear-layer characteristics.

All mean and fluctuating velocity data presented herein were obtained with a constant-temperature anemometer (TSI model 1050) with a tungsten wire probe ($l/D = 450$, $D = 0{\cdot}00015$ in.). A TSI linearizer (model 1055) was used to provide analog output signals proportional to velocity. This unit was calibrated *in situ* prior to initiating the current measurement programme. No corrections for probe size or transpiration cooling effects have been applied to the results herein. The present temperature data were measured with a resistance thermometer with a tungsten wire sensor ($D = 0{\cdot}00015$ in.) in the constant-current mode ($I = 3$ mA). Because of the anemometer feedback bridge the frequency response for all velocity results is better than 5 kHz whereas the temperature data are limited to an upper frequency response of 1 kHz, primarily as a result of the thermal mass of the wire sensor. Since most of the turbulent energy for the shear layer investigated herein occurs below 500 Hz the noted frequency responses are considered adequate. For the current spectra data an H/P 3590 A wave analyser as well as a SAICOR 52 B spectrum analyser were used. In general, results from the two analysers were comparable although the SAICOR unit proved to be more efficient in terms of processing time requirements. A similar finding was made in determining correlations both with a TSI correlator, model 1015C, as well as with SAICOR's model 43 correlation and probability analyser.

Intermittency results for the present fluctuation data were obtained through use of a Philco Ford's ADP-11 intermittency meter and a Tetronix model 549 storage oscilloscope. The technique followed was essentially the same as that described by Demetriades (1968*a*, *b*) in his discussion of turbulent-front measurements for the axisymmetric wake. By observing on the oscilloscope the stored sample of the instantaneous signal for a given measurement point, it was possible to adjust the turbulence trigger level in a consistent and repeatable manner. The 0–1 V d.c. output, proportional to the intermittency factor (percentage of time flow is turbulent), was then read directly on system recording equipment.

A schematic diagram of the fibre optics probe and associated electronics is shown in figure 6 and a sketch of the probe head is presented in figure 7. In practice, a steady light beam from a tungsten-filament lamp is split into two beams which are then chopped at 1 c/s by a rotating chopper wheel. The resulting alternating beams after passing through a no. 2C light filter with a lower cut-off wavelength of 3800 Å, are focused on the ends of two fibre optics pipes guided inside stainless-steel tubes. One of the pipes leads to a reference gap filled with air, whereas the other leads to the probe's measurement gap. The light sensor probe detects concentrations of NO_2 because of light attenuation in the probe gap caused by the passage of eddies of dark-brown NO_2 gas. From the gaps, the light beams are led to a photomultiplier tube

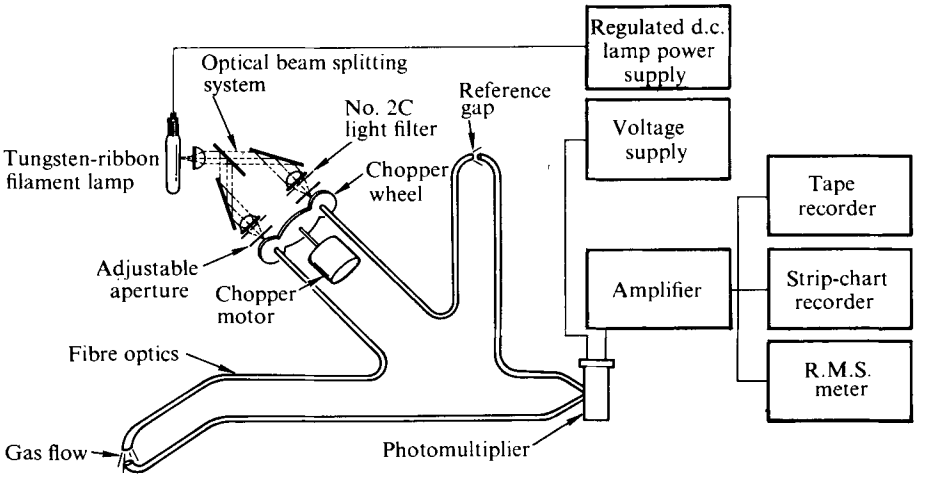

FIGURE 6. Schematic diagram of concentration probe.

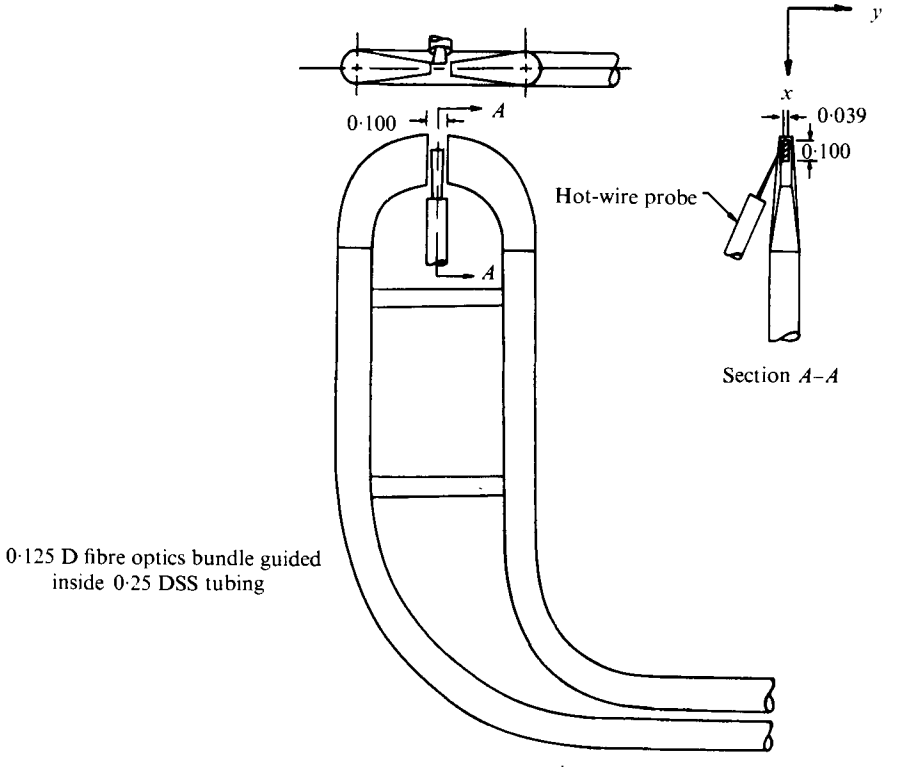

FIGURE 7. Temperature/concentration probe configuration. Dimensions in inches.

(RCA 931 A), where they are converted into electric signals before being amplified and fed into system recording equipment. While actual measurements were being performed, all experiments were conducted in complete darkness. All exposed probe supports and tunnel side walls were coated with non-reflecting black paint to minimize spatial resolution difficulties arising from the effects of stray scattered light.

The purpose of the chopper wheel, which is activated both before and after measuring a data sample, is to provide a means of monitoring the reference signal strength and thereby determining the extent of any light drift that may have occurred during the course of a measurement. In practice, with the probe at rest at a given position in the mixing region, the chopper-wheel motor is shut off in order to permit measurement over a sufficient time interval that conventional averaging techniques may be applied to the results. To isolate the ends of the fibre optics pipes from the nitrogen dioxide gas as well as to ensure even transmission of light, optically clear microscopic glass (0·003 in. thick) was bonded with Canadian Balsam cement to each face of the probe. Because of the absorption properties of nitrogen dioxide to light at a wavelength of 4000 Å, and since all other species in the flow are transparent to light at this wavelength, the light attenuation in the probe gap is a relative measure of the NO_2 concentration level. A quantitative measure of this light attenuation is given by Beer Lambert's law, which relates the transmission of light (I/I_0) to the prescribed optical path l_f and the concentration of the absorbing medium (NO_2) in the following manner:

$$I/I_0 = E/E_0 = 10^{-\beta l_f[NO_2]}$$

(Glasstone 1946; Lee & Brodkey 1963). After some rearranging it can be shown that, for the dilute concentrations used in the present experiments, the differences in photomultiplier voltage between the reference and attenuated signals are linearly related to the NO_2 concentration levels as follows:

$$\Delta E/E_0 = -2{\cdot}3\beta l_f[NO_2],$$

where β represents the molar extinction coefficient for nitrogen dioxide ($1{\cdot}33 \times 10^5$ cm^2/mole; Wegener 1959; Giauque & Kemp 1938; Hall & Blacet 1952) and l_f represents the probe gap size in the spanwise direction. Bench check calibration results confirmed the linearized version of the Beer Lambert law for the signal levels considered herein ($\Delta E/E_0 \leqslant 0{\cdot}05$), a result similarly observed by Lee & Brodkey (1963) in their light probe experiments.

Since microscales for the half-velocity ray of the half-jet (0·15 in.; Wygnanski & Fiedler 1970) are somewhat larger than characteristic probe dimensions (0·1 in., figure 7), the light sensor probe provides data of sufficient sensitivity and frequency response to furnish detailed information regarding the fine-scale structure of the flow field.† Shown in figure 7 is the hot-wire probe as positioned for simultaneous data measurements within the probe gap, but laterally displaced from the light sensor window towards the core-flow side of the jet by roughly 0·025 in. This lateral displacement from the light beam path was required in order to prevent disturbing the transmitted light beam signal. Note that the wire is aligned parallel to the light beam path and is positioned at the midpoint of the window length. For the probe design shown in figure 7 signal sensitivity levels $\Delta E([NO_2]/[N_2])^{-1}$ of 300 mV/% were achieved and a signal-to-noise ratio $E_{ref}/E_{noise} = 2500$ (E_{ref}–$E_{core}/E_{noise} = 100$) and a 5 % down frequency of roughly 2 kHz were realized. All concentration fluctuation data presented herein are shown corrected for random noise. It should also be mentioned that the fibre optics work of Nye & Brodkey (1967) and Lee & Brodkey (1963) as well as the results of

† In an original version of the probe design the gap size was set at 0·4 in. However, when intensity and spectra concentration data were suitably corrected for gap size (Rosensweig 1959) and random noise, measured results for the two probe sizes agreed to within 5 %.

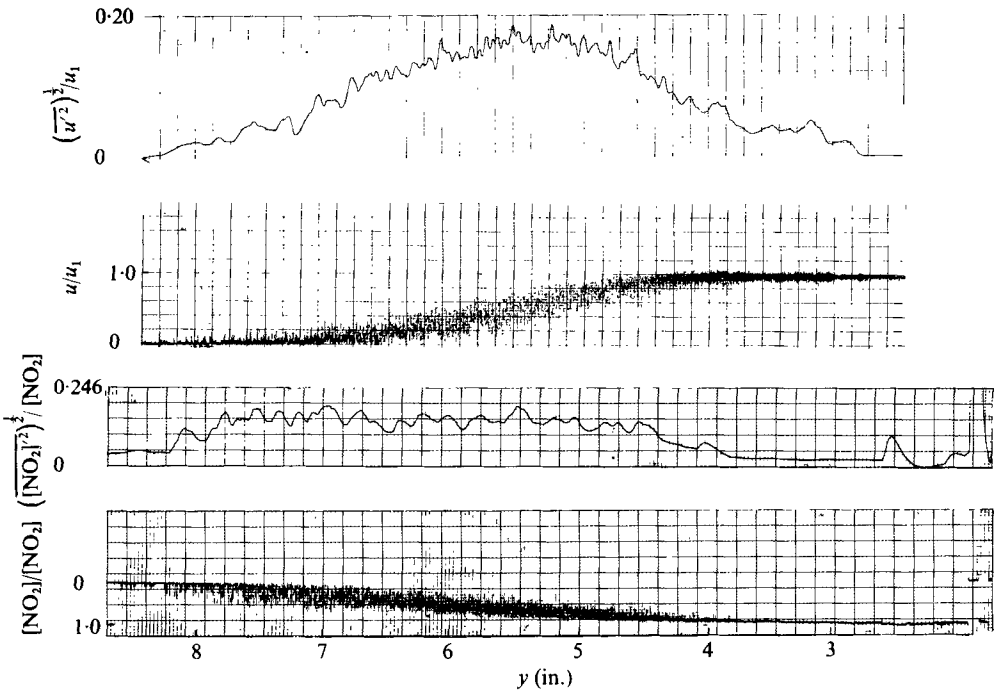

FIGURE 8. Typical time traces of concentration/velocity data across jet.

error analyses by Rosensweig (1959) were very helpful in satisfactorily developing the final design for the light sensor probe. The thorough light scatter experiments of Rosensweig, Hottel & Williams (1961) and Becker, Hottel & Williams (1967), who investigated a turbulent axisymmetric jet marked by oil smoke, were also very useful in helping to plan and perform the measurements discussed herein.

To illustrate output signal characteristics for the hot-wire and light sensor probes, typical raw data plots for instantaneous (but not simultaneous) velocity and passive-species signals, as recorded on oscillograph paper, are shown in figure 8. These data were obtained by separate traverses of the hot-wire and concentration probes across the jet from the ambient air to the primary side of the shear layer. Not only is the intermittent character of both signals evident near the shear-layer edges, but the concentration data display the expected one-sided character near the jet edges.

3. Passive-species mixing in a turbulent shear layer

In presenting the measured results which follow, an attempt has been made to relate the current data base to corresponding results of other investigators. Although such a comparison is not intended to be comprehensive, it does however serve the purpose of establishing the consistency of the present data relative to existing measurements. To this end table 1, representing a summary of test conditions and characteristic turbulence data for several types of free shear flow, has been prepared. Although most data entries reflect 'author suggested' values, certain of the results were interpreted and/or obtained indirectly from published data.

3.1. *Mean profiles*

Mean flow profiles of velocity, temperature and passive-species concentration (non-reacting $[NO_2]$ concentration at room temperature) are plotted in figure 9 as a function of the shear-layer similarity parameter

$$\eta = \sigma_R \frac{(y - y_{0.5})}{(x - x_0)},$$

where σ_R corresponds to the reference spreading parameter ($= 12$), $y_{0.5}$ represents the half-profile location and x_0 is the effective origin of the shear layer. The results illustrated were obtained at core-flow speeds of 23 and 50 ft/s and at axial distances varying from 10 to 25 in. Although a slight temperature difference ($\Delta T = 5$ °C) existed across the shear layer for the case where $T_1 = 305$ °K, the flow temperatures were sufficiently high to ensure that the oxides of nitrogen would occur only in the form of passive NO_2 concentrations. Effective origins x_0 for these data were based on the data on shear-layer thickness in figure 10, which shows the variation of tangent-slope thickness with axial distance.

When comparing the mean velocity and temperature data for the two-dimensional mixing region obtained by different investigators, measurable differences in profile shape become evident (figure 11, table 1). Excluding the data for high-speed ratios of Spencer & Jones (S & J, 1971), the primary reason for this apparent lack of universality in the shear layer's mean profile shape is believed to be the sensitivity of the shear layer to initial conditions and/or free-stream turbulence phenomena. Support for the viewpoint that such effects play a prominent role in the development of a shear layer's mean and turbulent flow field is provided not only by the measurements for coaxial jets of Ragsdale & Edwards (1965) and Boehman (1967) but also by the shear-layer studies of Bradshaw (1966), Chandrsuda *et al.* (1977), Batt (1975) and Oh & Bushnell (1975). In general these authors found that the shear layers' turbulent structure depends strongly both on the transitional nature of the initial boundary layer as well as on the amplitude and spectra (scale) of the external flow disturbances. The faster spread rate for the Wygnanski & Fiedler (W & F, 1970) data has in fact been shown (Batt 1975) to be the direct result of disturbing the initial boundary layer with a wire trip. Such a spreading rate corresponds to a spreading parameter σ of 9 as compared with the value of 12 for the Liepman & Laufer (L & L, 1947) results and the present data. The sensitivity of the shear-layer flow to initial and/or external flow conditions should also be recognized (measured) when evaluating the role played by orderly eddy structures in a fully turbulent shear layer (Chandrsuda *et al.* 1977). Although additional reviews and comparisons of shear-layer data have also recently been given by Champagne, Pao & Wygnanski (1976) and Dimotakis & Brown (1976), it is hoped that an appropriately detailed study of the turbulent mixing layer, including quantitative measurements as well as photographic results, will be carried out in the near future to resolve these fundamental and important shear-layer questions.

On examining the present mean profile data, the temperature and concentration profiles are seen to be nearly identical in form, thus implying that the Lewis number (L: ratio of eddy diffusivity for mass ϵ_m to eddy diffusivity for temperature ϵ_T) is approximately equal to one. The growth rates and the half-profile locations ($\eta_u = 0$, $\eta_T = \eta_{NO_2} = 0$) for the velocity and temperature/concentration data, however,

Flow	Author(s)	u_1	r	D (in.)	$\left(\frac{x}{D}\right)_{max}$	x_{max} (in.)	Re_D	Re_x (max)	$\frac{\delta_u}{x-x_0}$	$\frac{\delta_u}{\delta_T}$	σ/σ_R ($\sigma_R = 12$)	$\frac{L_x}{\delta_u}$	$\frac{L_y}{\delta_u}$
Isotropic turbulence	Theory	—	—	—	—	—	—	—	—	—	—	—	—
Plane wake (cylinder)	Townsend (1949)	42	—	0·375	160	—	$8·4 \times 10^3$	—	—	—	—	(0·83)	(0·32)
	Grant (1958)	20	—	0·125	533	—	$1·3 \times 10^3$	—	—	—	—	0·83	0·43
Plane jet	Bradbury (1965)	150	0·16	0·375	70	—	3×10^4	—	0·06	—	—	—	0·44 (0·38)
	Forthmann (1934)	110	—	0·25	12	—	$1·5 \times 10^5$	—	0·10	—	—	—	—
Round jet	Corrsin & Uberoi (1949)	65–115	—	1	25	—	7×10^4	—	0·08	0·81	—	(0·88)	0·25 (0·16)
	Gibson (1963)	4	—	6	50	—	$1·5 \times 10^4$	—	0·11	—	—	(0·75)	—
	Wygnanski & Fiedler (1969)	170	—	1	90	—	1×10^5	—	0·09	—	—	0·43 (0·43)	0·25 (0·18)
Mixing layer (round jet)	Lawrence (1956)	200–700	0	3·5	4	18	$1·4 \times 10^6$	7×10^6	0·18	—	—	0·52 (0·52)	0·21 (0·21)
	Bradshaw (1966)	300	0	2	4	8	4×10^5	$1·6 \times 10^6$	0·17	—	0·96	0·57	0·22
	Davies *et al.* (1963)	200–600	0	1	4	4	$1·5 \times 10^6$	6×10^6	0·18	—	0·96	(0·56)	(0·22)
	Kolpin (1964)	300–950	0	1	4	4	$5·5 \times 10^5$	$2·2 \times 10^6$	0·18	—	—	0·56	0·26
Mixing layer (plane jet)	Sunyach & Mathieu (1969)	59	0	1·6	3	4·8	5×10^4	$1·4 \times 10^5$	0·21	0·72	0·90	—	—
Mixing layer ($r > 0·1$)	Spencer & Jones (1971)	100	0·3	—	—	50	—	$2·5 \times 10^6$	0·090	—	1·8	0·46 (0·37)	0·22 (0·19)
		100	0·6	—	—	50	—	$2·5 \times 10^6$	0·038	—	4·2	0·45	—
	Brown & Roshko (1974)	50 (7 atm)	0·14	—	—	4	—	1×10^6	0·134	—	1·07	—	—
		50 (7 atm)	0·38	—	—	4	—	1×10^6	0·089	—	1·56	—	—
Mixing layer ($r < 0·1$)	Liepmann & Laufer (1947)	59	0	—	—	35	—	1×10^6	0·17	—	0·97	—	0·17
	Wygnanski & Fiedler (1970, with trip)	40	0	—	—	23	—	5×10^5	0·23	—	0·75	0·48 (0·48)	0·24 (0·24)
	Patel (1973)	85	0	—	—	40	—	$1·8 \times 10^6$	0·18	—	0·97	—	—
	Batt (1975, with trip)	50	0·03	—	—	26	—	7×10^5	0·23	—	0·75	—	—
	Present data	50	0·03	—	—	26	—	7×10^5	0·18	0·72	0·96	—	—
	Present data	23	0·07	—	—	28	—	$3·5 \times 10^5$	0·18	0·72	0·96	0·57	0·27

[TABLE 1 *continued on facing page*]

TABLE 1 (*cont.*)

Flow	Author(s)	$\frac{L_x}{L_y}$	$\frac{\Lambda_x}{\Lambda_y}$	$\frac{L_x}{\Lambda_x}$	$\frac{L_y}{\Lambda_y}$	$\frac{\tau_u u}{L_x}$	$\frac{\bar{\tau}_u u}{L_x}$	$\frac{\tau_T u}{\Lambda_x}$	$\frac{(\overline{u'^2})^{\frac{1}{2}}\dagger}{\Delta u}$	$\frac{(\overline{T'^2})^{\frac{1}{2}}}{\Delta T}$	$\frac{\overline{u'v'}\dagger}{\Delta u}$		$\frac{\overline{v'T'}\dagger}{\Delta u\,\Delta T}$	
											Data	∫‡	Data	∫‡
Isotropic turbulence	Theory	2	1·0	1·5	0·75	—	—	—	—	—	—	—	—	—
Plane wake (cylinder)	Townsend (1949)	2·6	—	—	—	—	—	—	—	—	—	—	—	—
	Grant (1958)	1·9	—	—	—	—	—	—	—	—	—	—	—	—
Plane jet	Bradbury (1965)	—	—	—	—	—	—	—	—	—	—	—	—	—
	Forthmann (1934)	—	—	—	—	—	—	—	—	—	—	—	—	—
Round jet	Corrsin & Uberoi (1949)	3·5 (5·5)	1·5 (3·0)	(1·7)	0·65 (0·85)	—	—	—	—	—	—	—	—	—
	Gibson (1963)	—	—	—	—	—	—	—	—	—	—	—	—	—
	Wygnanski & Fiedler (1969)	1·7 (2·4)	—	—	—	1·10	1·2	—	—	—	—	—	—	—
Mixing layer (round jet)	Lawrence (1956)	2·5	—	—	—	1·0	—	—	0·125	—	—	—	—	—
	Bradshaw (1966)	2·6	—	—	—	—	—	—	0·14	—	0·010	—	—	—
	Davies *et al.* (1963)	2·5	—	—	—	—	3·0	—	0·16	—	—	—	—	—
	Kolpin (1964)	2·2	—	—	—	0·85	—	—	0·125	—	—	—	—	—
Mixing layer (plane jet)	Sunyach & Mathieu (1969)	—	—	—	—	—	—	—	0·19	0·13	0·0135	0·0125	—	0·017
Mixing layer ($r > 0{\cdot}1$)	Spencer & Jones (1971)	2·0 (2·0)	—	—	—	—	5·5	—	0·185	—	0·013	0·128	—	—
		—	—	—	—	—	—	—	—	—	—	—	—	—
	Brown & Roshko (1974)	—	—	—	—	—	—	—	—	—	—	—	—	—
		—	—	—	—	—	—	—	—	—	—	—	—	—
Mixing layer ($r < 0{\cdot}1$)	Liepmann & Laufer (1947)	—	—	—	—	—	—	—	0·145	—	0·0080	0·0103	—	—
	Wygnanski & Fiedler (1970, with trip)	2·0 (2·0)	—	—	—	—	2·3	—	0·18	—	0·0090	0·0095	—	—
	Patel (1973)	—	—	—	—	—	—	—	0·175	—	0·0105	0·0105	—	—
	Batt (1975, with trip)	—	—	—	—	—	—	—	0·18	—	—	—	—	—
	Present data	—	—	—	—	—	—	—	0·17	—	—	—	—	—
	Present data	2·1	1·20	1·30	0·75	0·75	2·3	3·7	0·17	0·13	0·0113	0·0113	0·0105	0·0150

† Maximum value. ‡ Calculated by integrating mean flow profiles.

TABLE 1. Summary of turbulence data. Reference velocity: for jet, $u_1 = u_{\text{exit}}$ (ft/s); for mixing layer, $u_1 = U_{\text{core}}$ (ft/s). Speed ratio: $r = u_2/u_1$. Boundary-layer thickness: for jet, δ = half-velocity radius; for mixing layer, δ = tangent-slope thickness. Length (time) scales not in parentheses are e^{-1} decay distances (times). Length (time) scales in parentheses are integral length (time) scales.

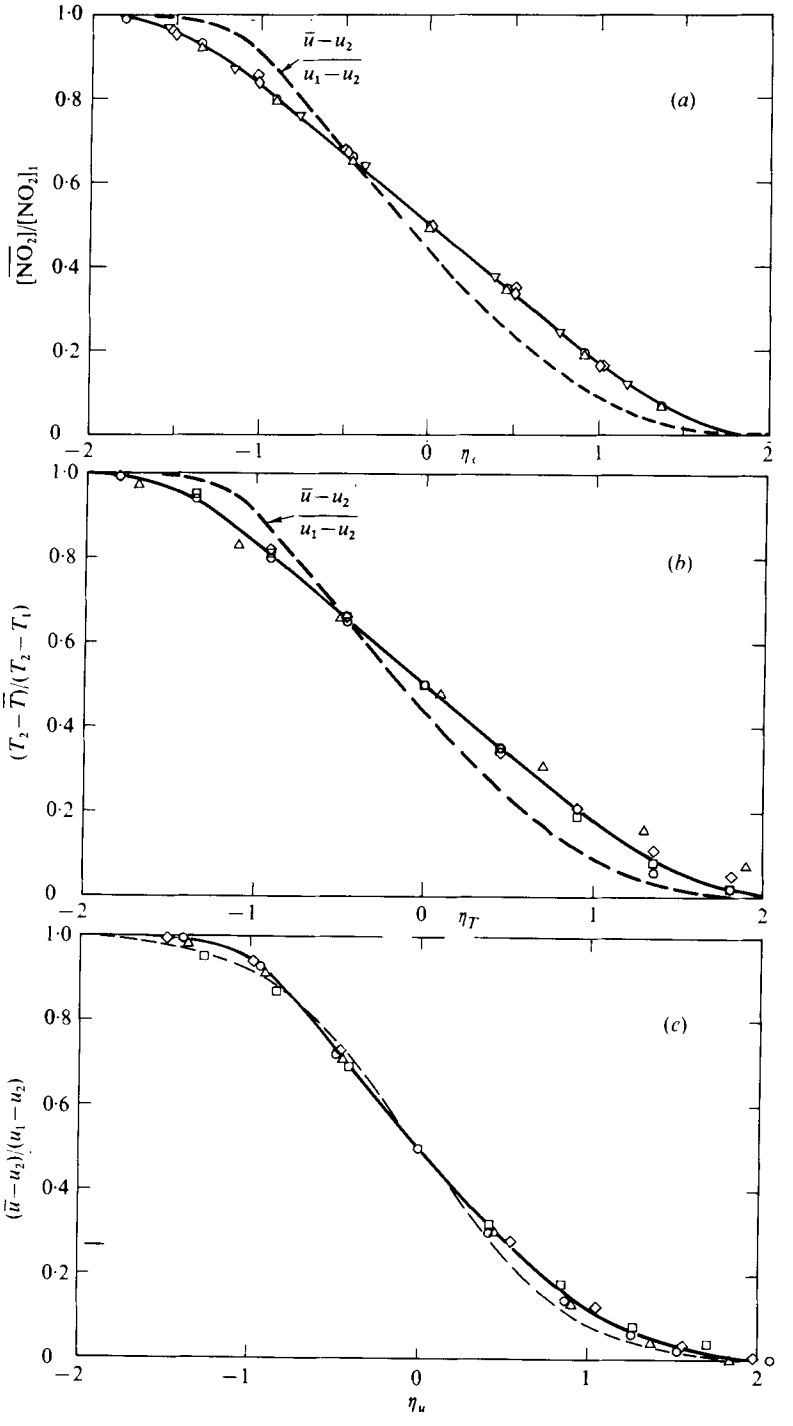

FIGURE 9. Mean profile distributions. For present data points in (*b*), $u = 23$ ft/s, $x - x_0 = 18{\cdot}5$ in. Dashed curve in (*c*) is $\frac{1}{2}(1+\operatorname{erf}\eta)$.

		○	◊	◇	▽	△	□
(*a*)	u (ft/s)	23	50	50	50	50	—
	$x-x_0$ (in.)	18·5	10·9	16·5	21·7	26·3	—
(*b*)	T_1 (°K)	273	—	305	—	—	252
	T_1/T_2	0·880	—	0·985	—	Sunyach	0·820
(*c*)	u (ft/s)	23	—	50	—	50	23
	$x-x_0$ (in.)	18·5	—	16·5	—	26·3	28·3

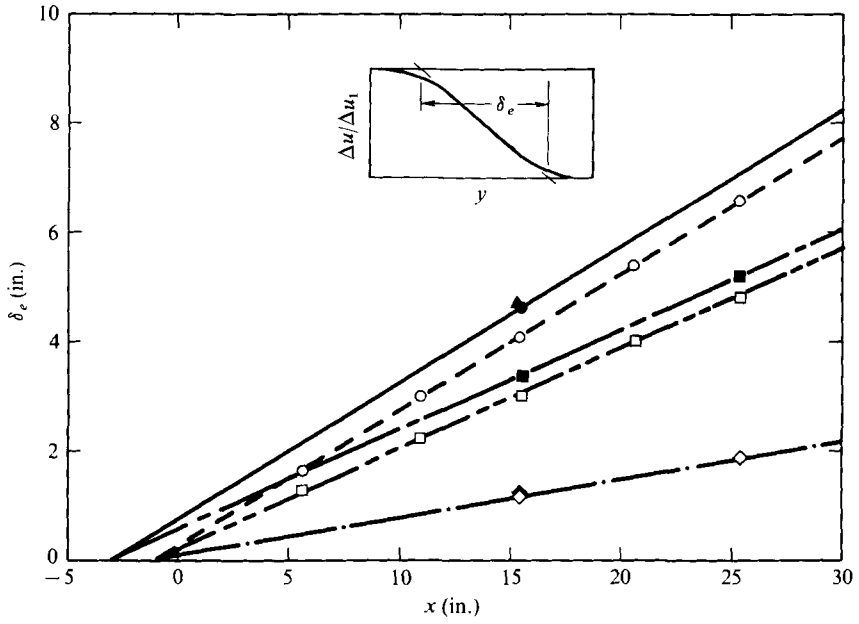

FIGURE 10. Thickness distribution summary. ○, $\overline{[NO_2]}/[NO_2]_1$; △, $(T_2-\bar{T})/(T_2-T_1)$; □, $(\bar{u}-\bar{u}_2)/(u_1-u_2)$; ◇, $r\bar{u}_c$ $(\eta_1 = 0)$; solid symbols, $u_1 = 23$ ft/s; open symbols, $u_1 = 50$ ft/s.

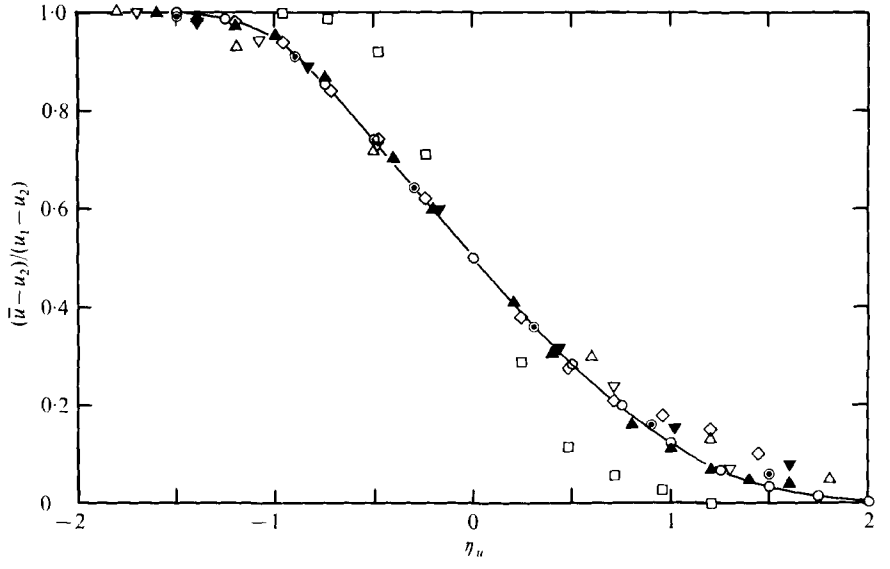

FIGURE 11. Comparison of mean velocity profiles. ○, present data; ▽, Sunyach (1971); △, W & F; ▲, L & L; ◇, Patel (1973); □, S & J, $r = 0{\cdot}3$; ⊙, Bradshaw (1966); ▼, Davies (1966).

differ considerably. By comparing these mean profile results, a turbulent Schmidt number (Sc_T: ratio of eddy diffusivity for momentum ϵ_u to eddy diffusivity for temperature ϵ_T) of approximately 0·5 is derived, which, although lower than results for axisymmetric flows (0·70; *Forstall & Shapiro 1950; Corrsin & Uberoi 1949*), agrees favourably with data for other two-dimensional flows. This low value for the Schmidt

number indicates the difference in transport mechanisms between scalar quantities and momentum as is evident also from the behaviour of the lateral spread exhibited in figure 10.

3.2. *Fluctuation intensities*

Intensity data for fluctuations in axial velocity, temperature, passive species and lateral velocity are presented in figure 12. The maximum velocity data compare favourably with results obtained by Spencer & Jones (1971) and by Jones, Planchon & Hammersley (1973) while the temperature data are in fair agreement with the measurements performed by Sunyach & Mathieu (1969). The concentration and temperature fluctuation data are nearly identical in both magnitude and profile shape, in noticeable contrast to the velocity intensity results. These data as well as the mean profile measurements discussed above support the finding from time-trace data (figure 8) that the lateral extent for passive scalars exceeds that for velocity. Note that the intensity profile for concentration fluctuations is 'flat topped' relative to the Gaussian-shaped results for velocity. It is also interesting to note from figure 8, as well as from the digital temperature and concentration data in figure 13, that the spikes in concentration fluctuation rarely exceed 50 % of the total concentration difference [NO_2]. This result is in substantial contrast to data measured by Brown & Roshko (1974) in their experiments on turbulent shear layers with density gradients and by Fiedler (1974, 1975) in his study of the temperature field within a plane mixing layer, which indicated that instantaneous density (temperature) fluctuations were often equivalent to the density (temperature) difference between the two external streams. Fiedler (1975) also measured maximum temperature intensities ($\simeq 20\,\%$) considerably larger than corresponding results for the current study ($\simeq 15\,\%$). This distinction between the present measurements and these earlier published data is considered significant and suggests that the turbulent mixing characteristics for the shear-layer experiments discussed herein were less influenced by coherent eddy structures (large-scale vortical motions) than were those in these previous investigations.

In reviewing the present fluctuation data a further interesting feature of the results is the velocity fluctuation distribution near the edge of the jet. Phillips (1955) has shown that the irrotational motion outside a turbulent boundary contains potential fluctuations which exhibit a linear dependence of $(\overline{u'^2}/\bar{u}_1^2)^{-\frac{1}{4}}$ on lateral distance. Measurements by Bradshaw (1967) and Wygnanski & Fiedler (1970) have shown that such behaviour occurs for the turbulent boundary layer and mixing region, respectively. The results presented in figure 14 verify that indeed the linear dependence exists for the present data.

An important step in processing/reducing the current set of data was accomplished by development of a digital data reduction program for the temperature and concentration data. From this program such statistical data as skewness and flatness factors have been determined and results are shown in figure 15. These data are similar in trend to velocity results reported by Spencer & Jones (1971). In the centre of the jet these data compare favourably with the Gaussian values for skewness (0) and flatness (3·0) and therefore suggest that probability densities in the jet centre are 'near' Gaussian.

3.3. *Probability density and spectra*

Examination of the probability density data presented in figure 16 further supports the 'near' Gaussian behaviour for the middle 50 % of the shear layer. On the other hand,

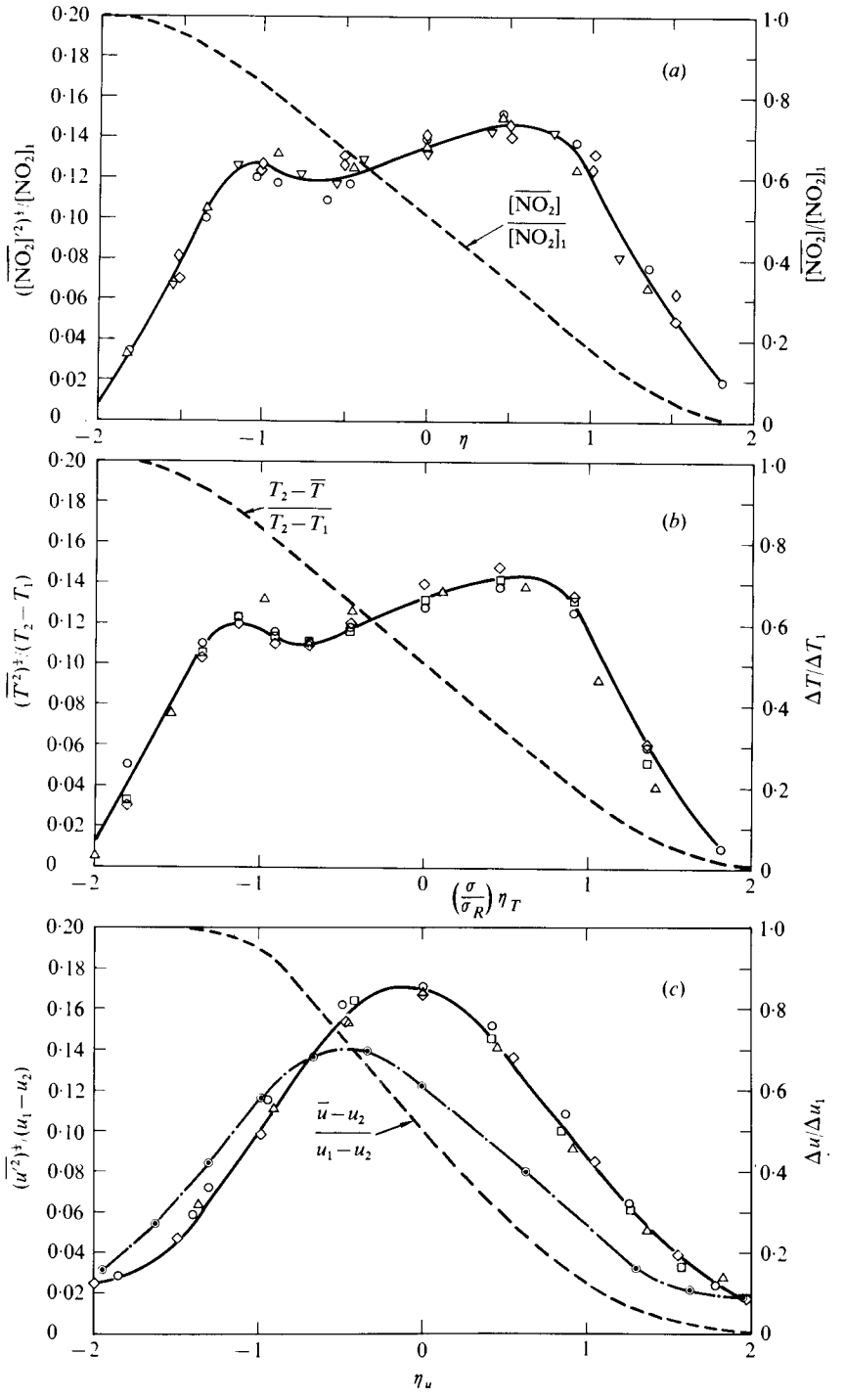

FIGURE 12. Intensity profiles. ⊙, $(\overline{v'^2})^{\frac{1}{2}}/(u_1-u_2)$, $u_1 = 23$ ft/s, $x-x_0 = 18{\cdot}5$ in. Other symbols as in figures 9(*a*), (*b*) and (*c*).

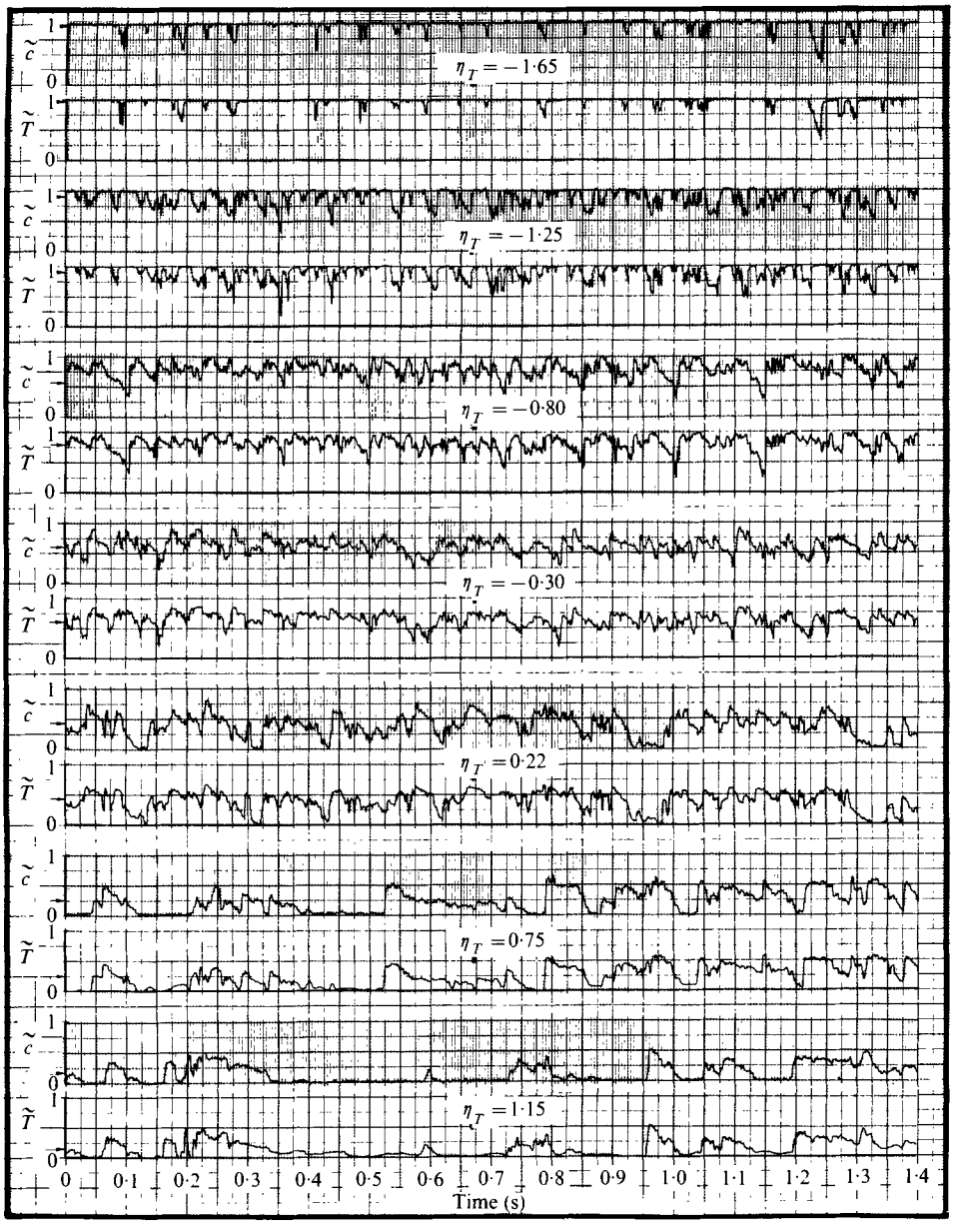

FIGURE 13. Digitized simultaneous time traces of temperature/concentration data ($T_1 = 305$ °K, $u_1 = 23$ ft/s).

a deviation from the Gaussian shape is evident near the jet edges for both temperature and concentration data. The bimodal character of the edge temperature/concentration data thus requires evaluation by those statistical theories which attempt to predict flow-field characteristics near shear-layer edges. An important result illustrated by the data in figure 16 is the absence of evidence that large-scale 'edge-to-edge' behaviour (jelly-roll mixing) is occurring in the shear layer studied herein. The abscissa scale factor in figure 16 shows the relative contributions to the probability density function

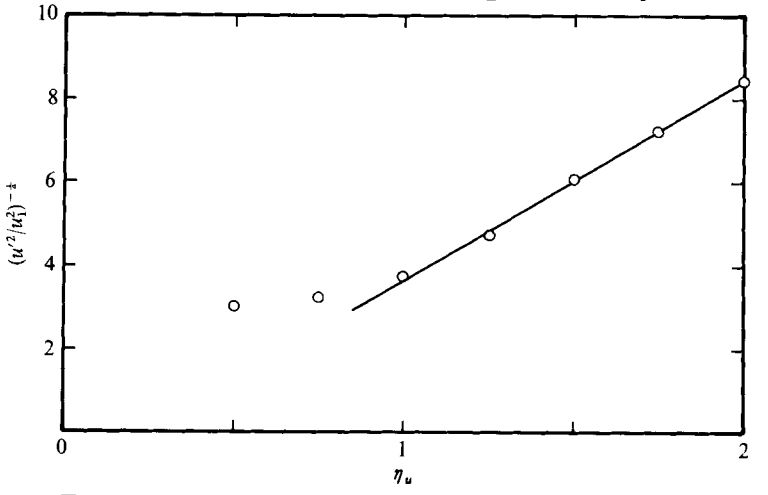

FIGURE 14. Velocity fluctuation near ambient edge of shear layer ($u_1 = 50$ ft/s, $x - x_0 = 16{\cdot}5$ in.).

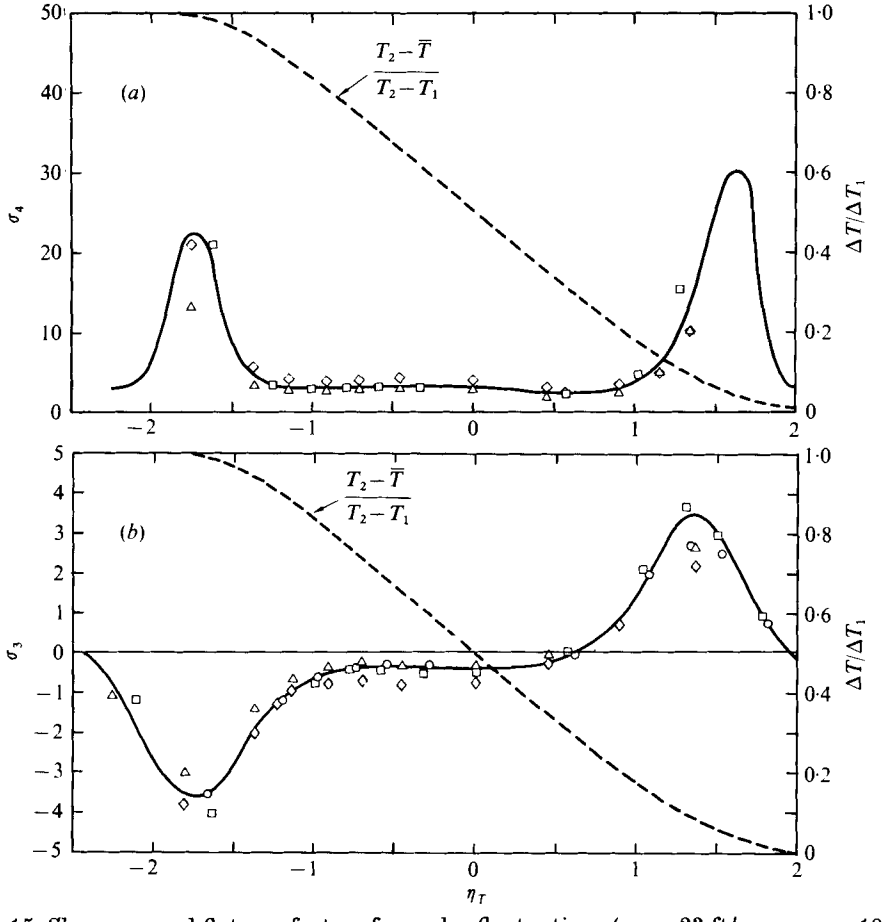

FIGURE 15. Skewness and flatness factors for scalar fluctuations ($u_1 = 23$ ft/s, $x - x_0 = 18{\cdot}5$ in.). (*a*) ◇, $\overline{T'^4}/(\overline{T'^2})^2$, $T_1 = 305$ °K; □, $\overline{T'^4}/(\overline{T'^2})^2$, $T_1 = 252$ °K; △, $\overline{[NO_2]'^4}/(\overline{[NO_2]'^2})^2$, $T_1 = 305$ °K. (*b*) ◇, $\overline{T'^3}/(\overline{T'^2})^{\frac{3}{2}}$, $T_1 = 305$ °K; ○, $\overline{T'^3}/(\overline{T'^2})^{\frac{3}{2}}$, $T_1 = 273$ °K; □, $\overline{T'^3}/(\overline{T'^2})^{\frac{3}{2}}$, $T_1 = 252$ °K; △, $\overline{[NO_2]'^3}/(\overline{[NO_2]'^2})^{\frac{3}{2}}$, $T_1 = 305$ °K.

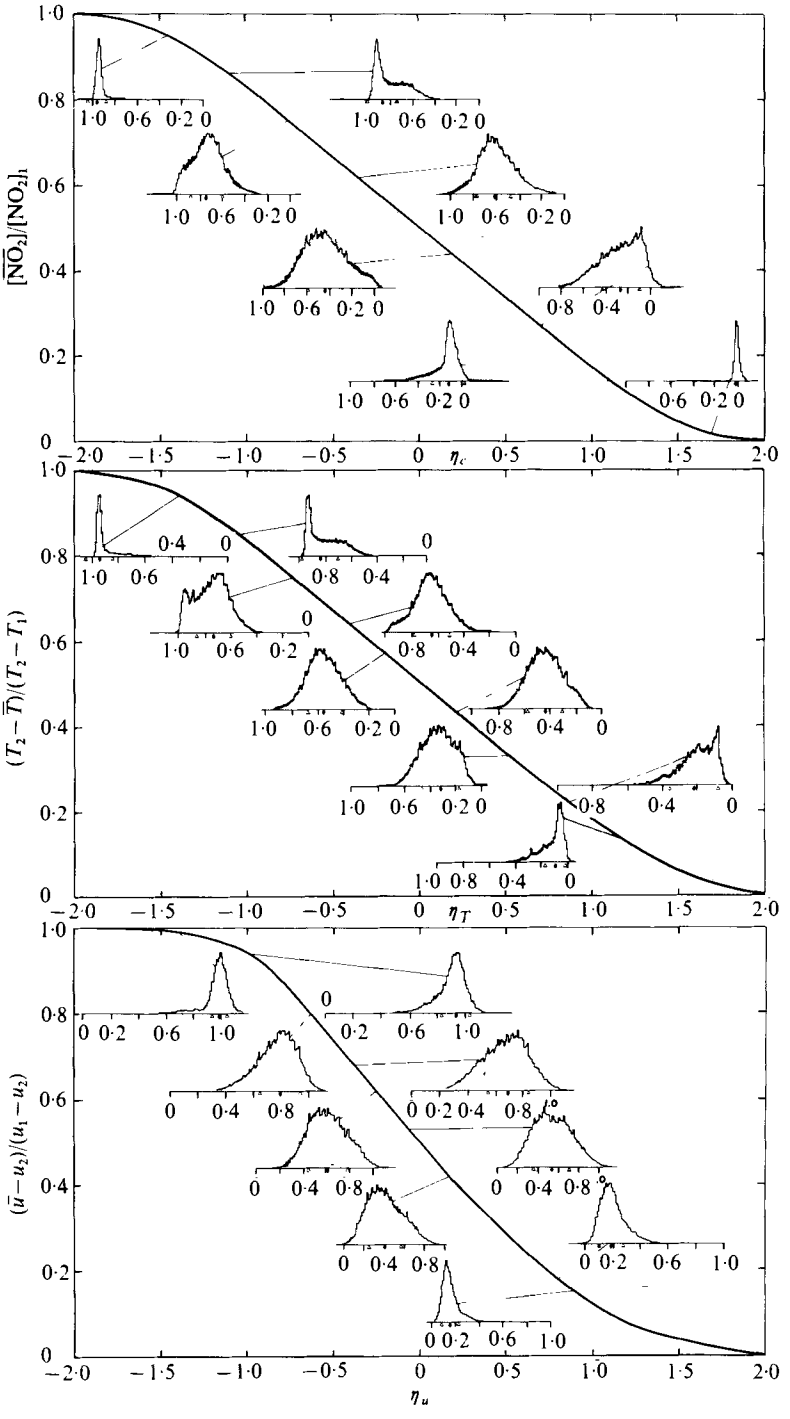

FIGURE 16. Dependence of probability density function on location within shear layer (u_1 = 23 ft/s, $x-x_0$ = 18·5 in.).

from eddies in different parts of the flow. The data point out that near the primary-flow edge negligible energy is associated with ambient air eddies and vice versa for measurements near the secondary edge of the shear layer. Such a result implies that the transport of edge fluid intact by large-scale motion plays a relatively minor role in the turbulent structure and mixing characteristics for the present shear layer. This result, which suggests that the measured data herein correspond to a fully three-dimensional turbulent shear layer, is supported not only by the photographic evidence of figure 4 and the time-trace data of figures 8 and 13, but also by the line-spectra data presented in figure 17 (plate 3) for an axial location $x-x_0 = 18{\cdot}5$ in. All data, as shown, exhibit relatively flat spectra shapes at low frequencies (large eddies), thereby substantiating that effects of flow periodicities occurring because of two-dimensional shear-layer instabilities are negligible. Although the spectra data of Spencer & Jones (1971) show 'spikes' at low frequency, these data also illustrate that the spike magnitude attenuates with decreasing speed ratio. In a similar manner low frequency spectral peaks were found to disappear with increasing Reynolds number in the supersonic turbulent shear-layer experiments of Ikawa & Kubota (1975). The dependence of the shear-layer structure on the Reynolds number, speed ratio and even on the density ratio (Brown & Roshko 1974) therefore appears to require further evaluation, as already suggested by Chandrsuda *et al.* (1977), Fiedler (1975) and Roshko (1976).

Summarized spectra results for velocity and passive-scalar [NO_2] concentration and temperature are presented in figures 18 and 19 in terms of power spectral densities and local wavenumbers normalized with a length scale based on the tangent-slope thickness (figure 10). Although concentration spectra data were measured at each of three locations at a given axial station (η at $u/u_1 = 0{\cdot}2$, $0{\cdot}5$ and $0{\cdot}8$), only data corresponding to the $u/u_1 = 0{\cdot}5$ location are shown since the three sets of data collapsed together and the half-velocity results represent a mean spectral distribution. The data in figure 18 indicate that normalizing the spectra in terms of a characteristic length scale, determined from a tangent-slope profile thickness, results in an approximate collapse of *all* data. An analytic representation for the mean distribution over a four-decade spread in power spectrum is given by the familiar k^{-2} formula:

$$\frac{E(k)}{q'^2\delta} = \frac{2}{\pi}\frac{L_x}{\delta}\frac{1}{1+(L_x/\delta)^2(k\delta)^2}. \tag{1}$$

The minor variations between the scalar and velocity spectra evident in figures 18 and 19 are consistent with measured magnitudes for normalized integral scales L_x/δ, to be discussed shortly, which were found to be larger for velocity data ($\simeq 0{\cdot}57$) than for temperature measurements ($\simeq 0{\cdot}27$). The present generally favourable agreement between scalar and velocity spectra was also noted by Corrsin & Uberoi (1949) in their temperature/velocity spectra in round heated jets and by Demetriades (1968*a*, *b*) in his density/velocity spectra data for an axisymmetric compressible turbulent wake. Although not shown, concentration and velocity data for core-flow fields of $u_1 = 23$ ft/s similarly agree with the results presented in figure 18. Because the turbulence Reynolds number ($Re_\lambda = u'\rho\lambda/u$) for the half-velocity location of the 50 ft/s results was small ($\simeq 40$) when based on the Liepmann–Laufer (1947) microscale and fluctuation data, it is not surprising that the Kolmogorov spectral law for an inertial subrange ($E_1(k_1) \sim k_1^{-\frac{5}{3}}$) applies, if at all, only for a very limited wavenumber range. The collapse of the concentration and velocity spectra data at large wavenumber suggests that the

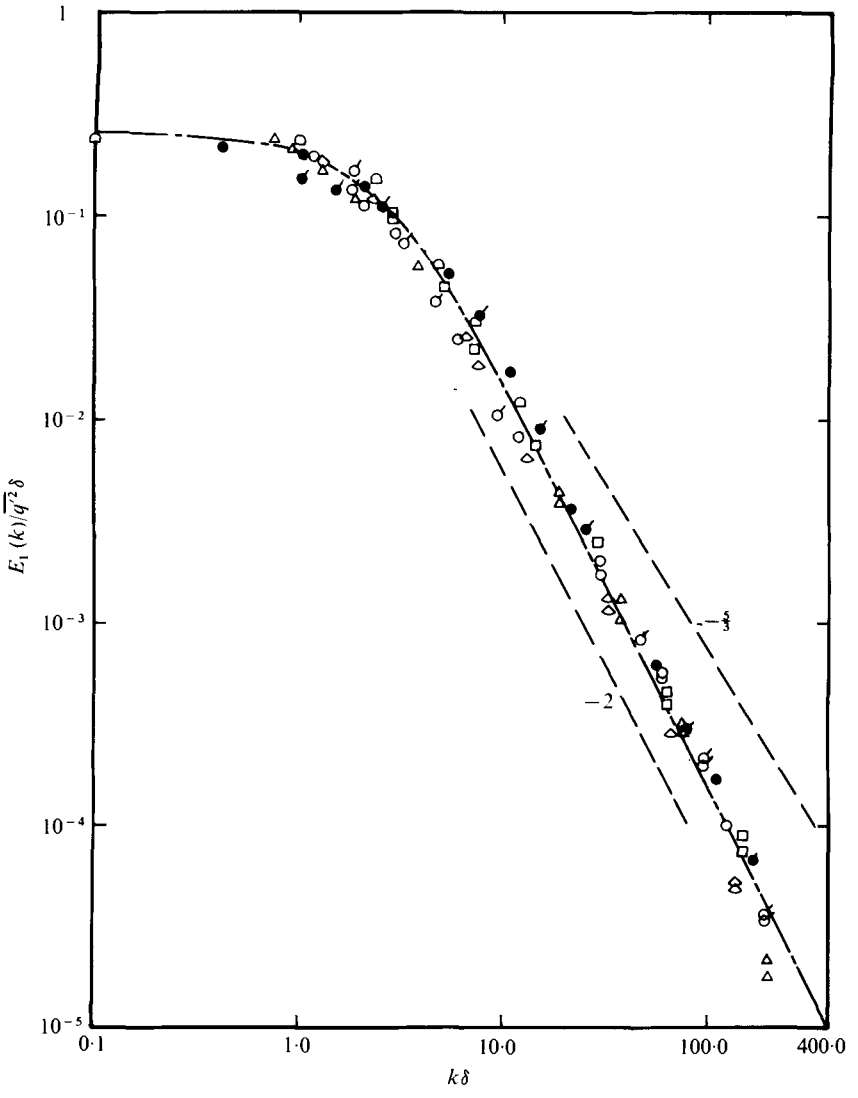

FIGURE 18. Summarized spectra results ($u_1 = 50$ ft/s). Open symbols, u'^2; solid symbols, $[NO_2]'^2$; flagged symbols, $x = 25{\cdot}3$; unflagged symbols, $x = 15{\cdot}5$; △, $\bar{u}/u_1 = 0{\cdot}8$; ○, $\bar{u}/u_1 = 0{\cdot}5$; □, $\bar{u}/u_1 = 0{\cdot}2$; ⬠, W & F, tripped mixing layer; ⬡, Batt, tripped mixing layer.

— · —, $\dfrac{E(k)}{\overline{q'^2}\delta} = \dfrac{2}{\pi}\dfrac{L_x}{\delta}\dfrac{1}{1+(L_x/\delta)^2(k\delta)^2}$, $\dfrac{L_x}{\delta} = 0{\cdot}4$.

fine-structure of the flow behaves in a homogeneous manner and that the microscale for longitudinal fluctuations remains roughly constant across the jet, a result also observed by previous investigators.

3.4. *Intermittency for velocity, temperature and concentration*

Intermittency profiles have been determined from the tape-recorded data for several locations in the shear layer. Typical oscilloscope traces used to obtain reduced data are shown in figure 20 (plate 4) and summarized results are presented in figure 21. The

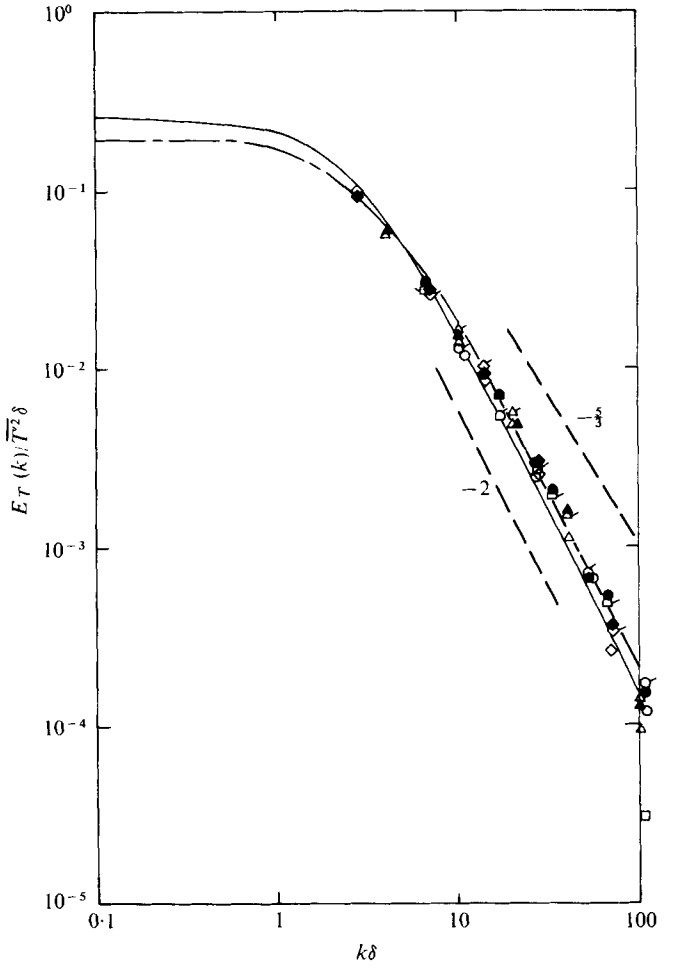

FIGURE 19. Temperature spectra ($u_1 = 23$ ft/s, $x = 15$). Open symbols, $T_1 = 305$ °K; flagged symbols, $T_1 = 273$ °K; solid symbols, $T_1 = 252°$ K.

Curves of $\dfrac{E(k)}{\overline{T'^2}\delta} = \dfrac{2}{\pi}\dfrac{L_x}{\delta}\dfrac{1}{1+(L_x^2/\delta)\,(k\delta)^2}$: ——, $\dfrac{L_x}{\delta} = 0{\cdot}4$; — · —, $\dfrac{L_x}{\delta} = 0{\cdot}3$.

	○	▭	△	◇	□
$(T_2-T)/(T_2-T_1)$	0·25	0·45	0·60	0·75	0·85

concentration/temperature data in figure 21 display a lateral extent comparable to that of the concentration intensity results in figure 12 and substantiate that similarity holds for these data. Although the comparison between the velocity and passive-scalar data is favourable on the primary side of the jet, a lack of agreement is evident at the jet's ambient air edge. Since the velocity data agree with results obtained by Wygnanski & Fiedler (1970, for $\sigma = 9$) and the scalar data compare qualitatively with the temperature measurements of Sunyach & Mathieu (1969), the noted discrepancy in velocity/scalar intermittency profiles was at first surprising. However, further study of the lateral extent of both mean and intensity profiles, as well as examination of simultaneous time traces such as those in figure 13, substantiates the present intermittency data. The simultaneous time-trace data in figure 22 (plate 5), for example,

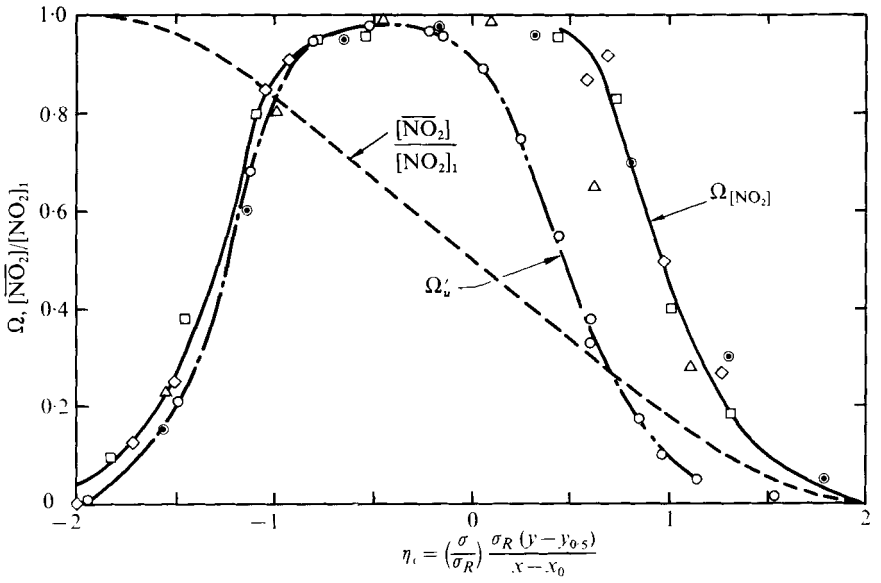

FIGURE 21. Intermittency factor summary. ◇, $[NO_2]'$, $u_1 = 50$ ft/s, $x-x_0 = 16{\cdot}5$ in.; □, $[NO_2]'$, $u_1 = 50$ ft/s, $x-x_0 = 26{\cdot}3$ in.; ○, u', $u_1 = 50$ ft/s, $x-x_0 = 16{\cdot}5$ in.; ⊙, T', $[NO_2]'$, $u_1 = 23$ ft/s, $x-x_0 = 18{\cdot}5$ in.; △, Sunyach.

show that the correlation of concentration with velocity and/or differentiated velocity is not exact, whereas excellent correlation exists between the concentration and temperature data. Noticeable in figure 22 is the intermittent character of the flow and the contrast between good correlation of velocity fluctuations with the scalar onset signal, but poor correlation with scalar-motion decay. A tentative explanation for this result, in addition to the well-known hot-wire sensitivity difficulty at low velocity, centres around the role of viscosity in selectively acting as a decay mechanism for velocity fluctuations, while having little or no effect on scalar motion. The pockets of fluid transported by bulk convection apparently experience probe passage times large compared with velocity decay times. Also exhibited in figure 22 is the dynamic character of the bulk convection motion at both the secondary and the primary edge of the jet. For example, the scalar onset signal near the low-velocity edge exhibits a sharp thermal leading edge (interface) in contrast to a relatively slow decay behaviour at the eddy trailing edge: a 'sawtooth' characteristic also evident, but more pronounced, in the temperature data of Fiedler (1974, 1975). This observed data trend, it should be noted, is consistent with the turbulent motion at the low-speed edge, which is characterized by eddies originating from the high-velocity region of the jet, which 'decay' in the vicinity of the probe. Similarly, just the opposite eddy motion was found to occur for eddies near the high-velocity edge (figure 13).

3.5. *Correlations*

Distributions of the Reynolds shear stress ($\overline{u'v'}/\Delta u^2$), the turbulent heat flux ($\overline{v'T'}/\Delta u\Delta T$) and the turbulent diffusivity of the mean-square temperature fluctuations ($\overline{v'T'^2}/\Delta u\Delta T^2$) are presented in figure 23. The turbulent shear-stress data were measured in the conventional manner with an X-wire probe whereas the latter two data sets were obtained by performing simultaneous measurements with an X-wire

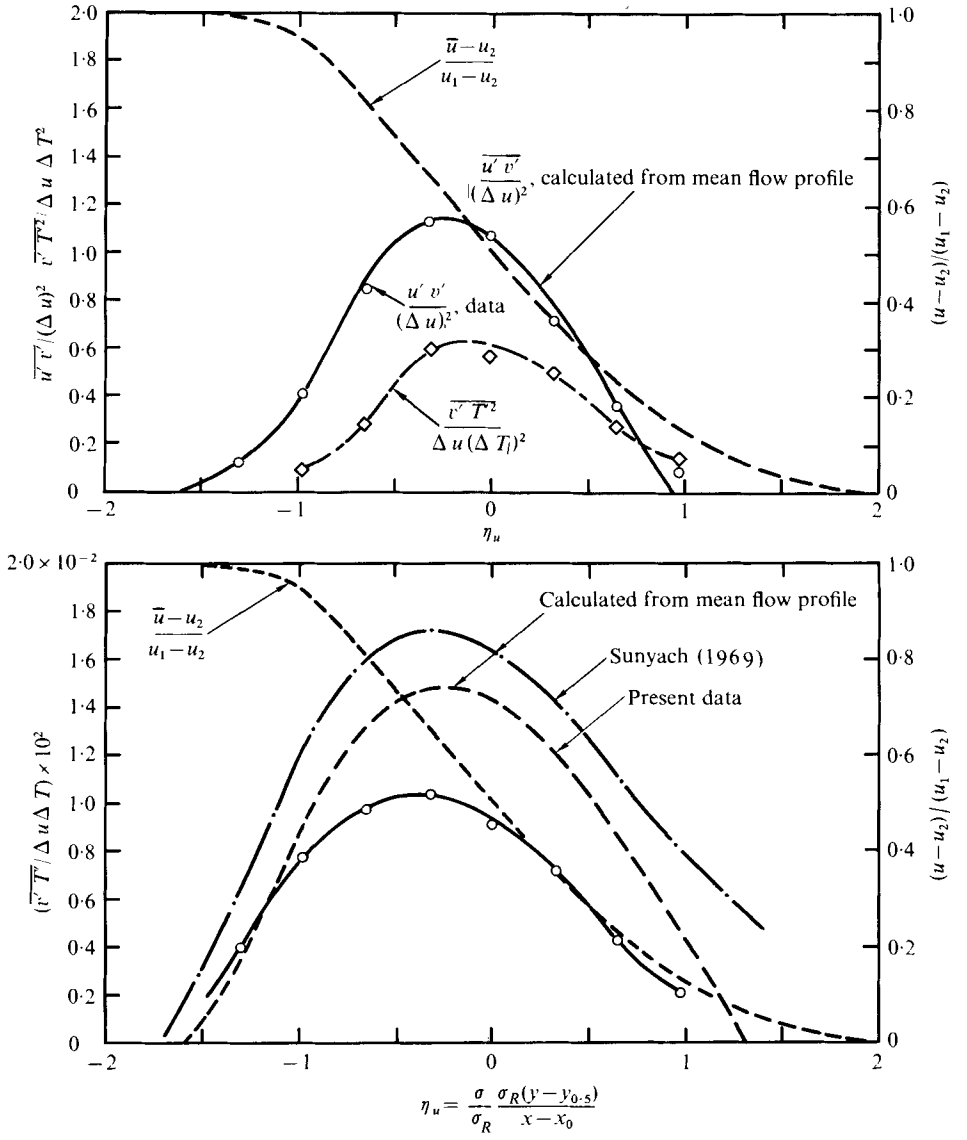

FIGURE 23. Shear-layer correlations (u_1 = 23 ft/s, $x-x_0$ = 18·5 in.).

probe and a single-wire temperature probe positioned just upstream (0·05 in.) of the X-wire probe. Although the present shear-stress measurements compare favourably with calculated shear data obtained from the mean flow profile, differences are evident when comparing the current results with measured data obtained by other investigators (figure 24 and table 1). Because of the measurement sensitivity of shear-stress data, however, the noted data spread is believed to be partially explained by the hot-wire experimental technique and/or moderate differences in test conditions.

Comparison of the measured heat-flux data $\overline{v'u'}/\Delta u \Delta T$ with the calculated heat-flux profile based on the mean flow data shows poor agreement (figure 23). Possible probe interference and/or displacement effects are considered responsible for this discrepancy.

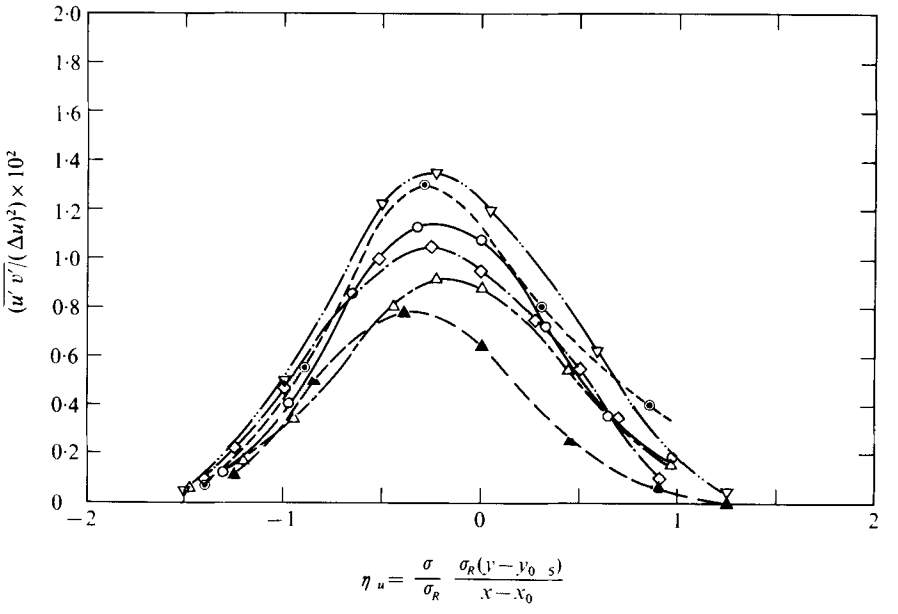

FIGURE 24. Shear-stress comparison. ○, present data; ▲, L & L; △, W & F; ◇, Patel; ▽, Sunyach; ⊙, Bradshaw.

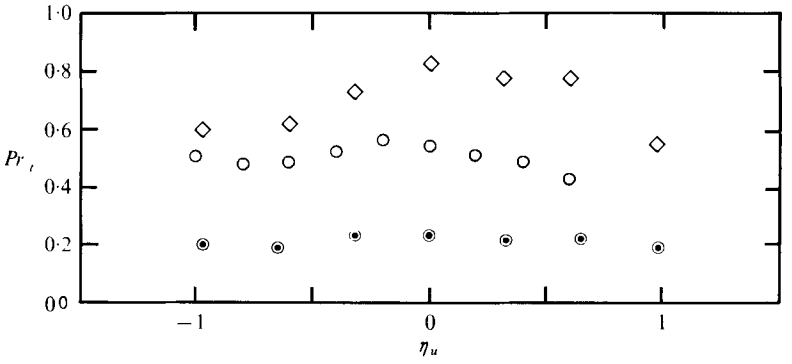

FIGURE 25. Turbulent Prandtl number within shear layer. ◇, based on measured $\overline{u'v'}$ and $\overline{v'T'}$; ○, calculated from mean flow profile; ⊙, $(\epsilon_u/\Omega_u) \times 10$.

This measurement difficulty is also most likely the reason why data on the turbulent Prandtl number

$$Pr_t \equiv \frac{\epsilon_u}{\epsilon_T} \equiv \left(\frac{\overline{u'v'}}{\partial u/\partial y}\right) \Big/ \left(\frac{\overline{v'T'}}{\partial T/\partial y}\right)$$

compare unfavourably with results based on mean flow profiles (figure 25). Note that the calculated value for Pr_t is approximately 0·5, in agreement with the tangent-slope thickness data in figure 10.

Normalized velocity and temperature correlations are also presented in figure 26 and it is of interest to note that these correlations never achieve magnitudes greater than 60 %. Shown also in figure 26 are coefficient results, determined from the digital data reduction program, for the correlation between temperature and passive NO_2 concentration. The near-unity levels exhibited by these data demonstrate that

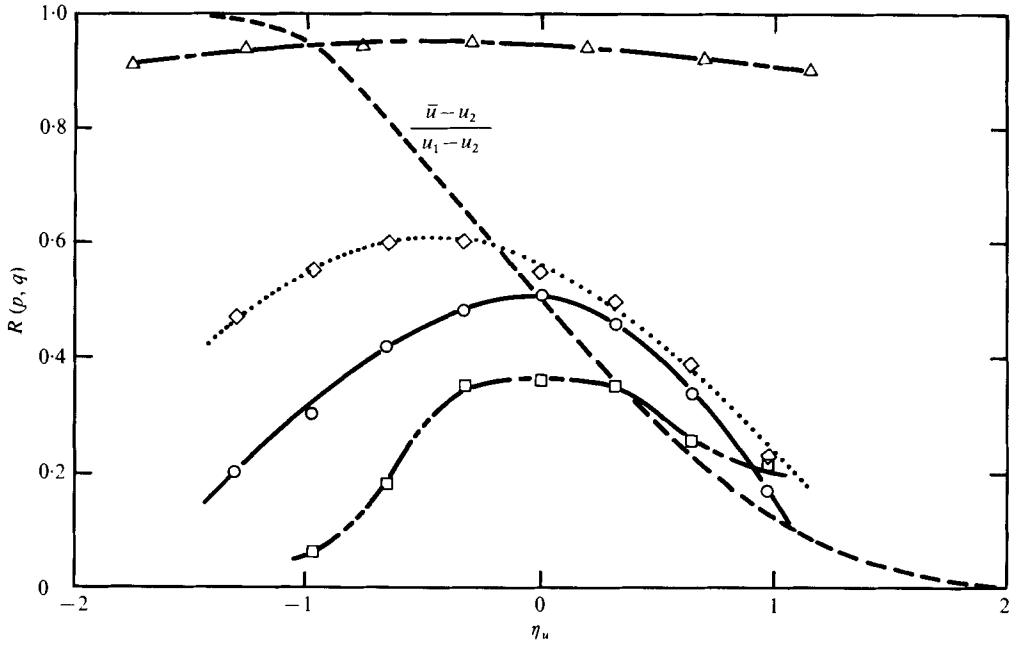

FIGURE 26. Shear-layer correlation coefficients (u_1 = 23 ft/s, $x-x_0$ = 18·5 in.). $R(p, q) \equiv \overline{p'q'}/(\overline{p'^2})^{\frac{1}{2}}(\overline{q'^2})^{\frac{1}{2}}$. ○, $R(u, v)$; ◇, $R(v, T)$; □, $R(v, T^2)$; △, $R([NO_2], T)$.

excellent correlation exists between a passive species and temperature in agreement with the time-trace data in figures 13 and 22. Such a result implies that not only is the Lewis number unity in a mean sense but also, instantaneously, the temperature and NO_2 signals behave identically.

3.6. *Space–time correlations*

To complete the data base for the present experimental investigation space–time correlation measurements of both velocity and temperature have been performed. In essence, the two-probe space–time correlation measurement technique with time delay (moving frame) is an attempt to bridge the gap between the Eulerian (probe fixed) and Lagrangian (fluid fixed) frames of reference. These measurements were undertaken to provide results describing not only the dependence of eddy size on location, but also the variation of eddy lifetime (moving-frame autocorrelation) and convection velocity with eddy size. The resulting data provide characteristic turbulent diffusion times which, when compared with chemistry times for the nitrogen tetroxide dissociation reaction, provide a means for assessing the non-equilibrium nature of the present chemically reacting experiments (§4).

Typical probe arrangements used to measure the required cross-correlation data are shown in figures 27 (*a*) and (*b*) (plates 6 and 7). These figures, which also show the smoke-seeded layer illuminated by a narrow beam of light projected in the axial direction, provide additional illustrations of the physical structure of the present turbulent mixing region. Note the presence of the two-dimensional coherent eddy structure near the origin of the mixing region as compared with the shear layer's random, turbulent and 'apparently' three-dimensional character further downstream.

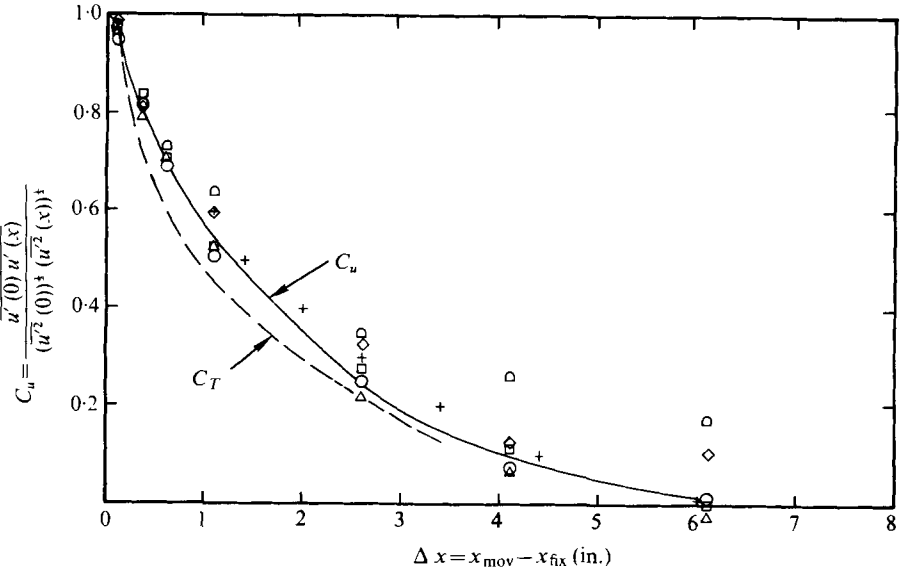

FIGURE 29. Axial velocity correlations (u_1 = 23 ft/s, $x_{\mathrm{fix}} - x_0$ = 18·5 in.). ○, $\eta_u = -0{\cdot}80$; △, $\eta_u = -0{\cdot}50$; □, $\eta_u = -0{\cdot}125$; ◇, $\eta_u = 0{\cdot}50$; ⌓, $\eta_u = 0{\cdot}125$; +, W & F.

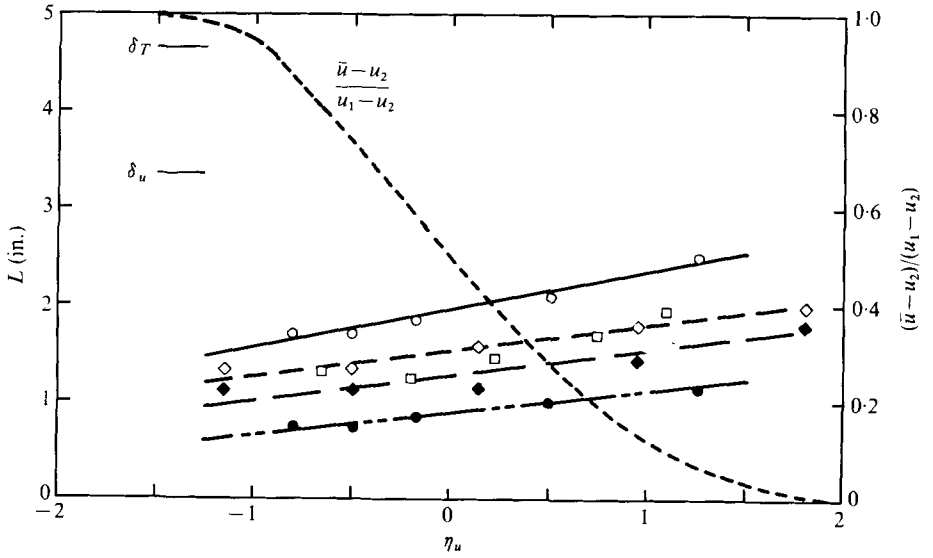

FIGURE 30. Lateral distribution of integral scales (u_1 = 23 ft/s, $x - x_0$ = 18·5 in.). ○, L_{xu}; ●, L_{yu}; ◇, L_{xT}; ◆, L_{yT}; □, τU_{ct}, $dR/dx = 0$.

The coherent-structure photographs in figure 27 were taken simultaneously with temperature oscilloscope traces which were triggered at times corresponding to the light source pulse. Not only do these data traces, for *short* axial distances, suggest flow periodicities and nearly frozen 'turbulence' (near the high-speed edge) but measured magnitudes indicate substantial penetration of edge fluid across the shear layer. Unfortunately, these and most other smoke photographs were taken after the major portion of the present experimental effort had been completed. If time had been available, additional measurements, including spanwise correlations as well as

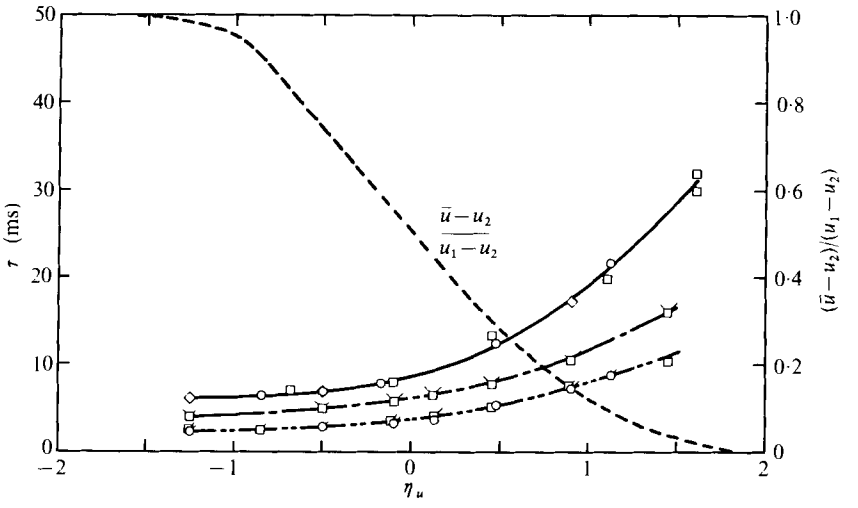

FIGURE 31. Lateral distribution of autocorrelation time scales.

	○ τ_u	♂ τ_u	◇ τ_T	□ τ_{NO_2}	♂□ τ_{NO_2}	♉ τ_{NO_2}
u (ft/s)	25	50	23	23	50	50
$x-x_0$ (in.)	18·5	18·5	18·5	18·5	16·5	26·3

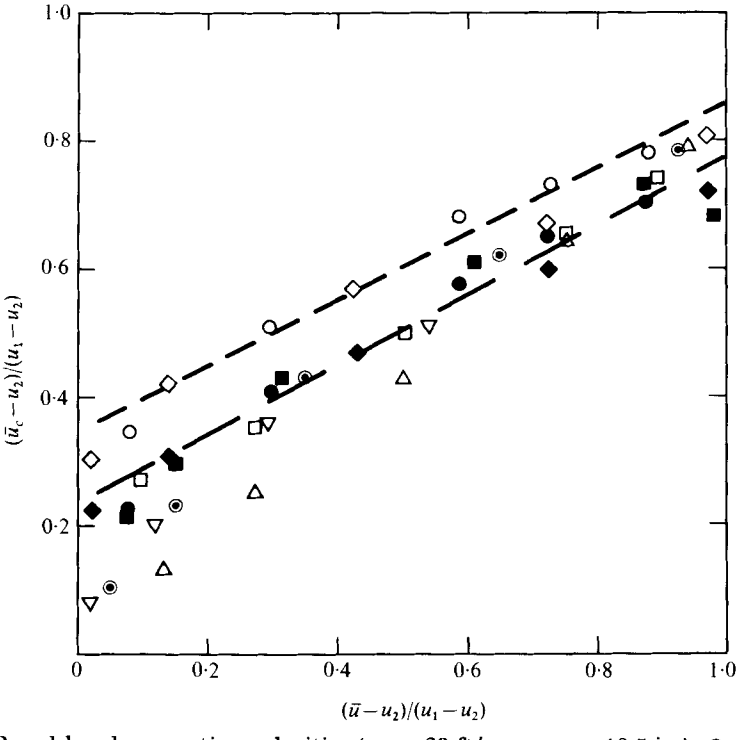

FIGURE 32. Broad-band convection velocities (u_1 = 23 ft/s, $x-x_0$ = 18·5 in.). ○, u, $dR/d\tau = 0$; ●, u, $dR/dx = 0$; ◇, T, $dR/d\tau = 0$; ◆, T, $dR/dx = 0$; □, Jones *et al.*; ■, Davies *et al.*; ⊙, Bradshaw; ▽, Wills; △, W & F.

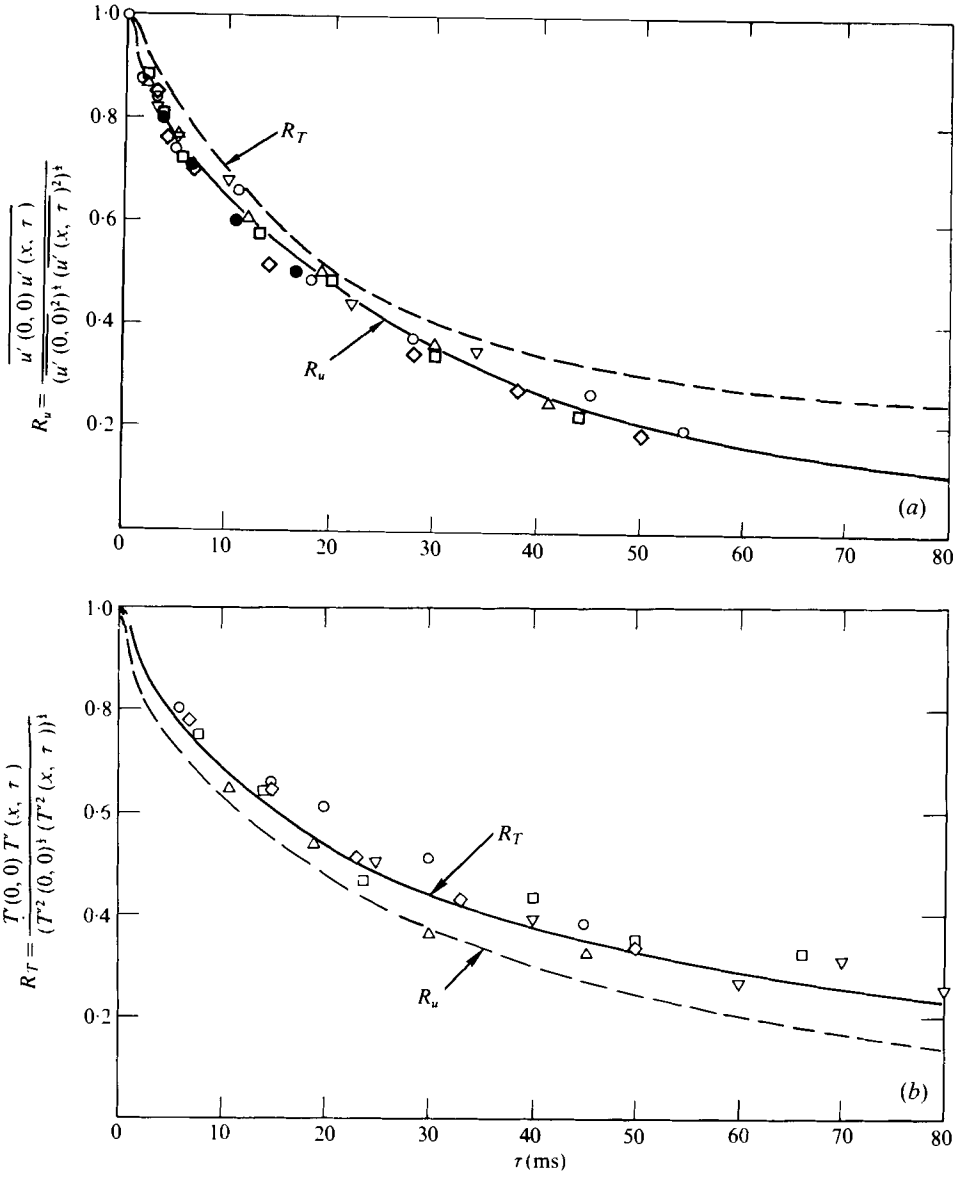

FIGURE 33. Broad-band moving-frame autocorrelation ($u_1 = 23$ ft/s, $x - x_0 = 18{\cdot}5$ in.) (*a*) $dR/d\tau = 0$. (*b*) $dR/dx = 0$.

		○	△	□	◇	▽	●
η_u	(*a*)	−0·77	−0·50	−0·17	0·50	1·20	W & F
	(*b*)	−1·15	0·15	0·95	−0·50	1·80	

detailed multi-probe measurements similar to the impressive results of Fiedler (1974, 1975), would have been desirable to determine the dependence of turbulent statistics on axial distance. Such an experimental study, which it is hoped will be carried out in the near future by other investigators currently studying shear-flow turbulence, would have provided a quantitative determination of the shear-layer development process to correspond with simultaneous still and motion-picture photographic

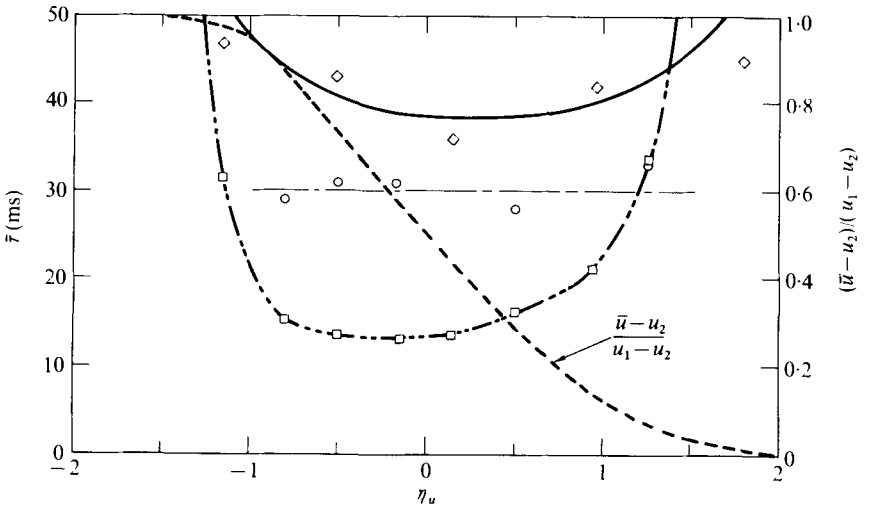

FIGURE 34. Moving-frame integral time scales (u_1 = 23 ft/s, $x-x_0$ = 18·5 in., dR/dx = 0). ○, $\bar{\tau}_u$; ◇, $\bar{\tau}_T$; □, $(d\bar{u}/dy)^{-1}$.

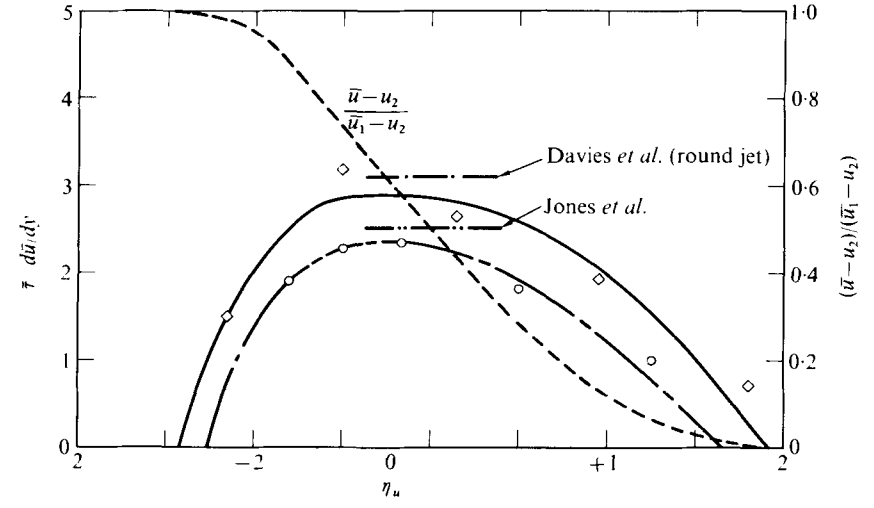

FIGURE 35. Normalized moving-frame integral time scales (u_1 = 23 ft/s, $x-x_0$ = 18·5 in., dR/dx = 0). ○, $\bar{\tau}_u\ d\bar{u}/dy$; ◇, $\bar{\tau}_T\ d\bar{u}/dy$.

results. In this manner an important clarification of the breakdown behaviour and the significance of orderly eddy structures might be determined.

Typical oscilloscope traces of temperature cross-correlations are shown in figure 28 (plate 8). Note that these correlations do not display the strong negative correlation found by Fiedler (1974) in his mixing-layer temperature measurements. Such negative correlation suggests the presence of some periodic motion in the Fiedler data, a possibility consistent with his large temperature intensities (20 %) and with the indication that edge fluid penetrated completely across the shear layer (Fiedler 1975).

By replotting the present axial cross-correlation coefficients corresponding to zero time delay as a function of probe separation, the eddy size dependence on shear-layer lateral location is obtained as shown in figure 29. The velocity data compare favourably

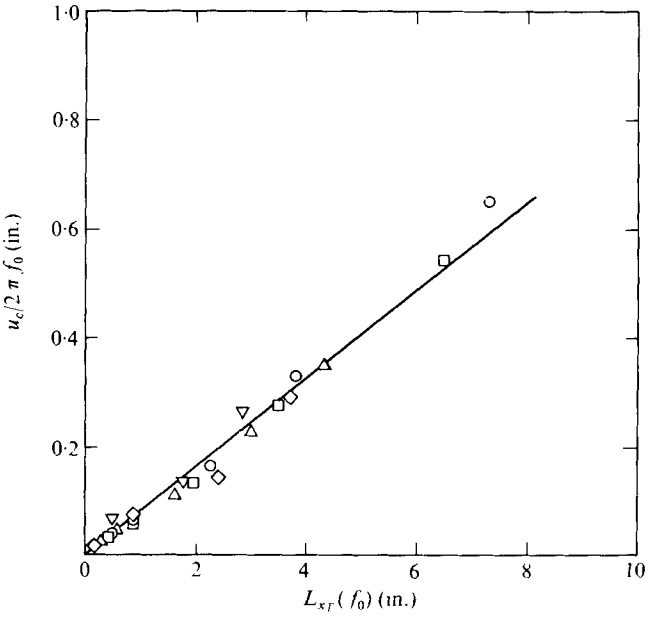

FIGURE 36. Filtered integral scales for temperature eddies ($u_1 = 23$ ft/s, $x - x_0 = 18{\cdot}5$ in.). ○, $\eta_u = -1{\cdot}15$; □, $\eta_u = -0{\cdot}50$; △, $\eta_u = 0{\cdot}50$; ◇, $\eta_u = 0{\cdot}95$; ▽, $\eta_u = 1{\cdot}80$.

with results obtained by Wygnanski & Fiedler (1970) both in magnitude and in the trend of increasing eddy size (integral scale) with movement towards the secondary-flow or low-speed side of the jet.

Derived velocity/temperature integral-scale data, based on the e^{-1} decay distance, are summarized in figure 30. Examination of these data illustrates that the velocity eddies ($L_y/L_x \simeq 0{\cdot}45$) appear to be 'stretched' relative to the temperature eddies ($\Lambda_y/\Lambda_x \simeq 0{\cdot}72$). Also the temperature axial scales are seen to compare favourably with a scale approximation (Taylor's hypothesis) based on the product of the autocorrelation time τ (figure 31) and the local convection velocity $\bar{u}_c$ (figure 32).

Typical unfiltered moving-frame autocorrelation results for the present investigation are shown in figure 33. These normalized data were obtained by plotting the peak correlation as a function of the time delay τ_D. e-folding moving-frame times $\bar{\tau}$ (eddy lifetimes) of the order of 30–40 ms are seen to be appropriate for the current study. It is interesting to note that, although temperature integral scales are somewhat smaller than the velocity scales, temperature eddy lifetimes tend to be longer than corresponding eddy lifetimes based on velocity data (figure 33). Again, data from measurements by Wygnanski & Fiedler (1970) compare favourably with the current velocity results. Because the present investigation involves a study of the interplay between chemistry and turbulence (§4), it should be noted that the integral time scales (30–40 ms) are large in comparison with typical chemistry times ($\leqslant 1$ ms). This comparison suggests that the energy eddies in the flow are in near chemical equilibrium. On the other hand, near the core-flow side of the jet, estimated dissipation times are of the same order as the chemistry times. Non-equilibrium effects may therefore be occurring on the dissipation scale in the present investigation.

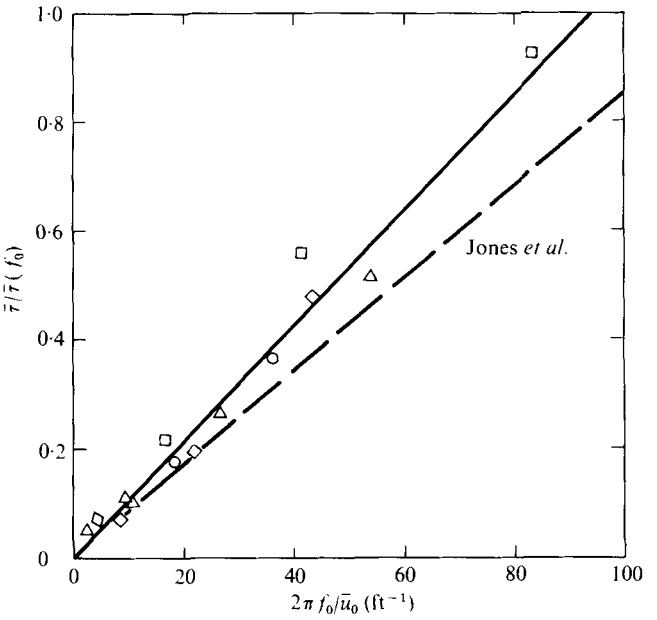

FIGURE 37. Filtered moving-frame integral time scales for temperature eddies (u_1 = 23 ft/s, $x-x_0$ = 18·5 in., dR/dx = 0). Symbols as in figure 36.

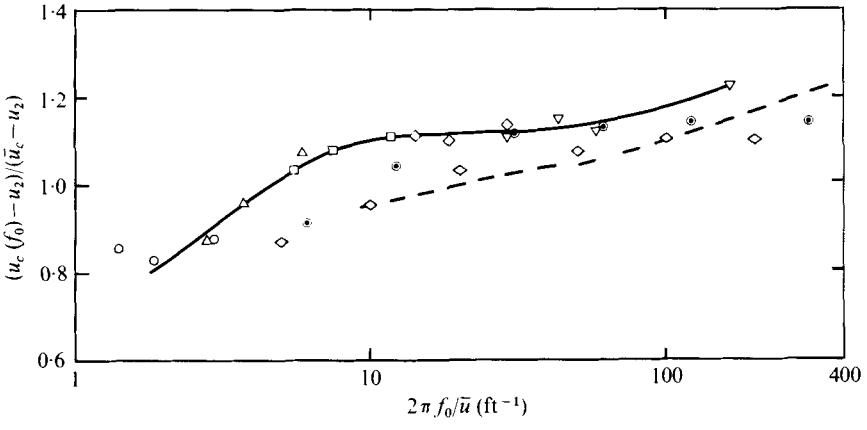

FIGURE 38. Filtered convection velocities for temperature eddies (u_1 = 23 ft/s, $x-x_0$ = 18·5 in.). f_0 (*c/s*): ○, 5; △, 10; □, 20; ◇, 50; ▽, 100. ---, W & F, round jet; ⊙, W & F, tripped mixing layer, ◇, Jones *et al.*, r = 0·3.

Often convective time scales are compared with Townsend's (1956), characteristic time for a free shear layer, based on the mean strain rate, i.e. $(d\bar{u}/dy)^{-1}$. This time scale is also shown in figure 34 and the current data are presented again in figure 35 normalized by this characteristic time for mean deformation. Near the mid-jet location, the present normalized time data agree favourably with results obtained by Davies *et al.* (1963) and by Jones *et al.* (1973). However, as found by the latter authors, and by Wygnanski & Fiedler (1970), the noted scaling did not hold across the shear layer.

Filtered moving-frame data for the eddy size, eddy lifetime and convection velocity are plotted as a function of wavenumber in figures 36, 37 and 38 respectively. These

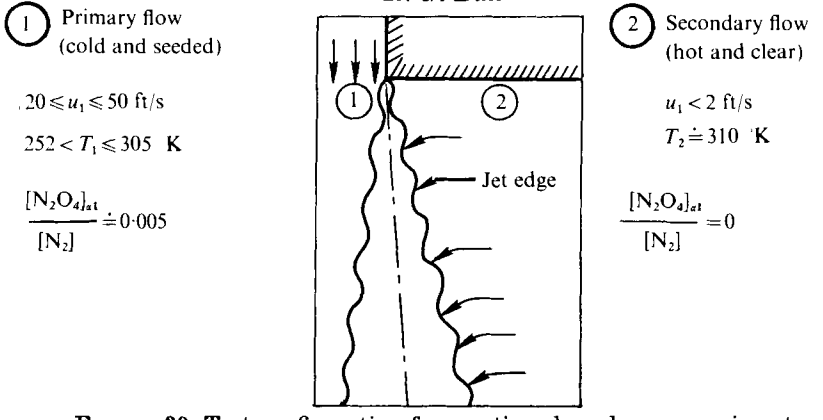

FIGURE 39. Test configuration for reacting shear-layer experiments.

data were obtained by first processing the data through narrow band-pass filters (f_0) and then correlating the filtered signals. The envelope of the family of resulting correlation curves then served as the filtered moving-frame autocorrelation. The data in figures 36 and 37 substantiate the general correspondence between eddy size/lifetime and a fixed frame frequency. The data in figure 37 further point out that lifetimes for even the small eddies are still large relative to appropriate chemistry times ($\leqslant 1$ ms) for the present chemically reacting experiments.

4. Mixing of chemically reacting species in a turbulent shear layer

4.1. *Mean flow profiles*

A schematic diagram of the shear layer and a list of the ranges of test conditions covered in the present reacting jet experiments ($N_2 + N_2O_4 \leftrightarrow 2NO_2 + N_2$) are shown in figure 39.† Measured mean NO_2 concentration profiles for the three temperatures investigated herein (T_1 = 252, 273 and 305 °K) are presented in figure 40. To minimize the possibility that the fibre optics probe thermally interfered with the tetroxide dissociation reaction locally, all reduced data correspond to results which were obtained only after the optics probe had been positioned for a sufficient time interval (10–15 s) to provide stable time-trace results. The reactant-product (NO_2) profiles shown in figure 40 for T_1 = 252 and 273 °K are seen to be displaced from the passive-species results corresponding to T_1 = 305 °K. The other curves presented in figure 40 represent calculated equilibrium NO_2 concentrations based on either measured *mean* ($\bar{T}$) or (using a digitized data analysis program) measured *instantaneous* (T) temperature data. It should be noted that the concentration measurement accuracy in the low-temperature case is roughly $\pm$ 10 % of the core-flow concentration levels. To gain further insight into the significance of the discrepancy between mean NO_2 data in figure 40 and the equilibrium predictions for T_1 = 252 °K, a discrepancy which was originally considered to be indicative of some non-equilibrium effects, several analytical models have been evaluated.

For the calculated results in figure 40 the equilibrium solution for the tetroxide dissociation reaction was derived through use of standard boundary-layer approximations and by noting that the production rate for the total oxide mass fraction is zero, i.e.

$$\dot{w} = \dot{w}_{N_2O_4} + \dot{w}_{NO_2} = 0,$$

† The basic experimental approach is reviewed in some detail in §2.

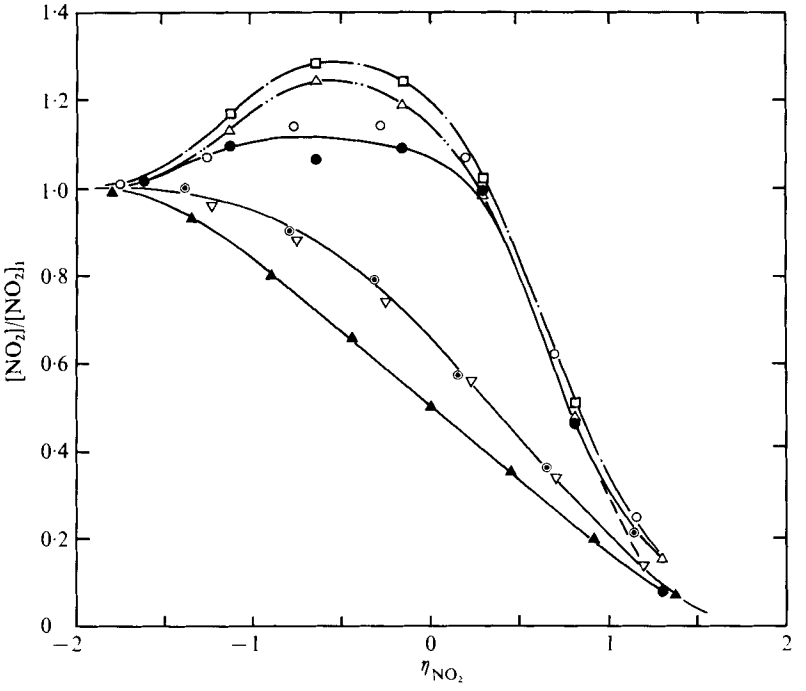

FIGURE 40. Mean concentration profiles for reacting shear layer ($u_1 = 23$ ft/s, $x - x_0 = 18{\cdot}5$ in.).

	Measured			Calculated			
	●	⊙	▲	△	▽	□	○
T_1 (°K)	252	273	305	252	273	252	252
				T	T	$\bar{T}$	T
				$L = 1$	$L = 1$	$L = 1$	$[N_2O_4]_a = [NO_2]_{M_{305}}$

where $$w = w_{N_2O_4} + w_{NO_2} = [N_2O_4]M_{N_2O_4} + [NO_2]M_{NO_2}.$$

It therefore follows that the species conservation equation for the total oxides of nitrogen can be written as

$$u\,\partial w/\partial x + v\,\partial w/\partial y = \epsilon_m\,\partial^2 w/\partial y^2.$$

The solution to this equation with the boundary conditions

$$w(-\infty) = w_1, \quad w(+\infty) = 0$$

is given by

$$w/w_1 = \tfrac{1}{2}(1 - \operatorname{erf} Sc_T^{\frac{1}{2}}\eta_w)$$
$$= \tfrac{1}{2}(1 - \operatorname{erf} Pr_T^{\frac{1}{2}}\eta_T) \quad \text{since (§3.1)} \quad \eta_T = \eta_w \quad \text{for} \quad L = 1.$$

To obtain values for w_{NO_2} and $w_{N_2O_4}$ use is made of the chemical equilibrium condition

$$k_D[N_2O_4][N_2] = k_R[NO_2]^2[N_2],$$

where $$K_c = k_D/k_R = \frac{1}{82T}\exp\left(27{\cdot}72 - \frac{6747}{T}\right) \quad \text{(Wegener 1959).}$$

Therefore, after some rearranging, the equilibrium solution for $[NO_2]$ in terms of mole fractions becomes

$$\frac{[NO_2]}{[N_2]}\left(1 + \frac{2[NO_2]}{K_c(T)}\right) = \frac{2[N_2O_4]_{a1}}{[N_2]}\frac{w}{w_1},$$

where $w/w_1 = [N_2O_4]_a/[N_2O_4]_{a1}$

and (1) $w/w_1 \simeq \frac{1}{2}(1-\text{erf}\, Pr_T^{\frac{1}{2}}\eta_T)$, $L = 1$, theoretical,

(2) $w/w_1 \simeq (T_2-T)/(T_2-T_1)$, $L = 1$, passive-scalar approximation

or (3) $w/w_1 \simeq ([NO_2]/[NO_2]_1)_{\underset{305}{M}}$, passive-species approximation.

Here Pr_T = turbulent Prandtl number and $[N_2O_4]_a/[N_2O_4]_{a1}$ = normalized molar concentration of total nitrogen oxides available for dissociation. The calculated data curves presented in figure 40 are based on the noted equilibrium solution result and as such correspond to the two-dimensional turbulent boundary-layer equations and include the assumptions that the eddy-viscosity and eddy-diffusivity coefficients are independent of the transverse co-ordinate but linearly dependent upon axial distance. Note that digitized data results are available for calculated $\overline{[NO_2]}/[NO_2]_1$ profiles based on measured temperature data only ($L = 1$, case 2) as well as on temperature and non-reacting $[NO_2]/[NO_2]_1$ data (case 3) for the passive-species run condition ($T_1 = 305\,°K$). The $[N_2O_4]_a/[N_2O_4]_{a1}$ time history for these latter results is thus represented by the passive $[NO_2]/[NO_2]_1$ data instead of through use of the temperature data and a Lewis number of unity. The resulting calculated results in figure 40 are seen to be in more favourable agreement with measured data than the instantaneous-temperature results for $L = 1$.

These analyses, it should be noted, were originally considered to be only approximate in nature since non-equilibrium phenomena were unaccounted for. Detailed finite-difference calculations† based on the homogeneous mixing model for the reacting mixing region were therefore carried out which took into account the interplay between finite-rate chemistry and fluid-mechanical convection and diffusion. These calculated results, although not shown, compare favourably with predicted concentration profiles based on mean temperature data and are determined by solving the species conservation equation

$$\bar{u}\frac{\partial\overline{[NO_2]}}{\partial x} + \bar{v}\frac{\partial\overline{[NO_2]}}{\partial y} = \overline{[\dot{N}O_2]} + \epsilon\frac{\partial^2\overline{[NO_2]}}{\partial y^2},$$

where $$\overline{[\dot{N}O_2]} = 2k_D(\bar{T})\,\overline{[N_2O_4]}\,\overline{[N_2]} - 2k_R(\bar{T})\,\overline{[NO_2]}^2\,\overline{[N_2]}$$

for fluid-mechanical similarity (as measured) but non-similar and non-equilibrium chemistry. The finite rates used in the net source term were based on mean temperatures and concentrations. On comparing these finite-rate results with mean temperature equilibrium predictions, the species profiles were found to be 'near' equilibrium in character.

One further attempt was made to account analytically for the observed measurement/prediction discrepancy in figure 40 by including second-order effects in the net source term of the species conservation equation. This was accomplished by formally time averaging the source term

$$\overline{[\dot{N}O_2]} = 2\overline{k_D[N_2O_4]\,[N_2]} - 2\overline{k_R[NO_2]^2\,[N_2]}$$

through use of the standard time-averaged representation of turbulent flow properties

$$T = \bar{T} + T', \quad k = \bar{k} + k', \quad [\ ]_i = [\ ]_i + [\ ]_i',$$

† The author is indebted to Dr Eric Baum for his assistance in formulating the finite-difference mathematics for these calculations.

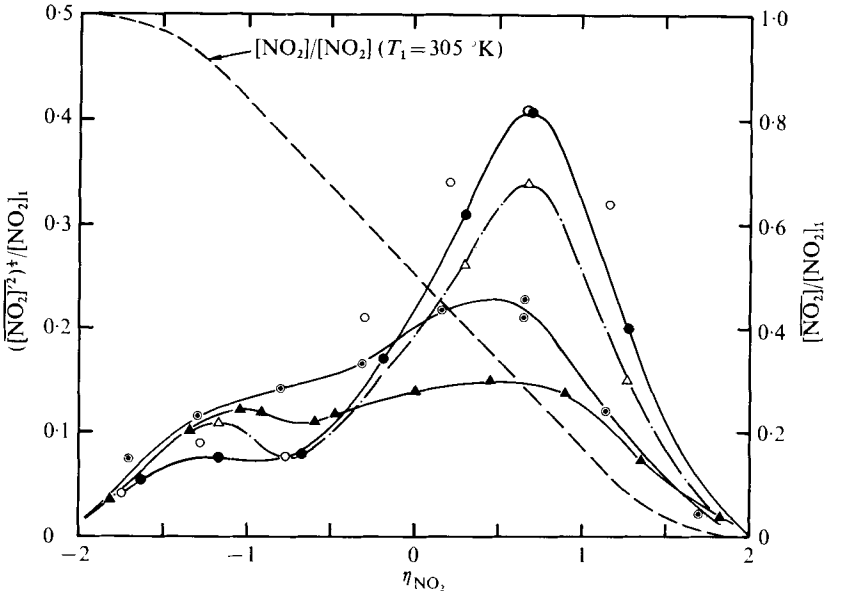

FIGURE 41. Concentration intensity profiles for reacting shear layer (u_1 = 23 ft/s, $x - x_0$ = 18·5 in.). Symbols as in figure 40.

and expanding both the forward and reverse rates in Taylor series:

$$k = k(\bar{T}) + \left(\frac{\partial k}{\partial T}\right)_{\bar{T}} T' + \frac{1}{2}\left(\frac{\partial^2 k}{\partial T^2}\right)_{\bar{T}} T'^2 + \ldots,$$

$$\bar{k} = k(\bar{T}) + \left(\frac{\partial^2 k}{\partial T^2}\right)\frac{\overline{T'^2}}{2} + \ldots,$$

$$k' = \left(\frac{\partial k}{\partial T}\right)_{\bar{T}} T' + \left(\frac{\partial^2 k}{\partial T^2}\right)_{\bar{T}}\left(\frac{T'^2 - \overline{T'^2}}{2}\right).$$

The source term then becomes

$$\begin{aligned}\frac{\overline{[NO_2]}}{2[\overline{N_2}]} = {} & k_D(\bar{T})\,\overline{[N_2O_4]} - k_R(\bar{T})\,\overline{[NO_2]^2} + \left(\frac{\partial^2 k_D}{\partial T^2}\right)_{\bar{T}}\frac{\overline{T'^2}}{2}\,\overline{[N_2O_4]} \\ & + \left(\frac{\partial k_D}{\partial T}\right)_{\bar{T}}\overline{T'[N_2O_4]'} + \left(\frac{\partial^2 k}{\partial T^2}\right)_{\bar{T}}\frac{\overline{T'^2[N_2O_4]'}}{2} \\ & - \left(\frac{\partial^2 k_R}{\partial T^2}\right)_{\bar{T}}\frac{\overline{T'^2}}{2}(\overline{[NO_2]^2} + \overline{[NO_2]'^2}) \\ & - 2\overline{[NO_2]}\left(\frac{\partial k_R}{\partial T}\right)_{\bar{T}}\overline{T'[NO_2]'} - \left(\frac{\partial k_R}{\partial T}\right)_{\bar{T}}\overline{T'[NO_2]'^2},\end{aligned}$$

with the first two terms representing the familiar 'laminar' or effective rate expression based on mean temperature. The additional terms include not only contributions due to temperature and species intensities but also double and triple correlations between temperature and species. Since the noted intensities and double correlations have been determined from measured data and, further, since estimates of triple-correlation magnitudes showed that such contributions were negligible, a second-order correction

to the laminar rate results was accomplished. It was found that although certain individual terms were as much as 15–20 % of the effective rate terms, the overall result of inclusion of the second-order terms was to modify the laminar rate calculation of mean concentration by approximately -5 %. Not only does this negligible correction effect provide an interesting validation of the laminar rate prediction technique, at least for the test conditions and chemical reaction considered herein, but this result further substantiates the equilibrium nature of the current experimental results. It is worthy of note also that this equilibrium conclusion is consistent with the large magnitude for measured eddy decay times (30 ms) compared with typical chemistry times ($\leqslant 1$ ms).

4.2. *Fluctuation intensities*

As was found for mean concentration profiles, concentration fluctuation intensities for the chemically reacting shear layer ($T_1 = 252$ °K) were significantly altered owing to chemistry. These data are shown in figure 41 along with the passive-species data described previously (§ 3.2). The equilibrium calculations discussed above similarly determined concentration intensities for this lowest-temperature case from the measured instantaneous temperature data. In general, favourable agreement in both shape and magnitude is evident on comparing these calculated results with measured data.

4.3. *Time-trace data*

One final interesting set of results has been developed through use of the digital analysis program. As previously described, this program calculates instantaneous properties of the shear layer and thus provides a means of automatically plotting normalized time-trace data. Typical such data are shown in figures 42 and 43 for core-flow temperatures of $T_1 = 252$ and 305 °K respectively. The middle trace in each figure corresponds to measured concentration data whereas the data for the lowest trace represent temperature results. The top trace on the other hand shows concentration data for $T_1 = 252$ °K based on the instantaneous equilibrium calculation using either temperature data only ($L = 1$, figure 42) or temperature data plus the assumption that

$$[N_2O_4]_a/[N_2O_4]_{a1} = [NO_2]_{\underset{305}{M}}/[NO_2]_1$$

(figure 43). For both figures the calculated equilibrium concentration data for the lower temperature ($T_1 = 252$ °K) are seen to compare favourably with measured data for this case. This result additionally verifies that the present reacting-shear-layer data correspond to a dissociation reaction in near chemical equilibrium, a finding which is further analysed and evaluated by Alber & Batt (1976). As noted in § 1, this latter paper reviews in some detail not only the current equilibrium chemistry data but also the passive-species results described in § 3. The main thrust of the present paper, it should again be noted, has been to document in a comprehensive manner the bulk of the measured results. The reader is therefore referred to the paper by Alber & Batt (1976) for examples illustrating the manner in which solutions to problems of current interest may be derived through use of empirical findings from the present experimental effort.

I am indebted to Dr Irwin Alber and to Professors Toshi Kubota and John Laufer for their support, interest and assistance during the course of this investigation. I am

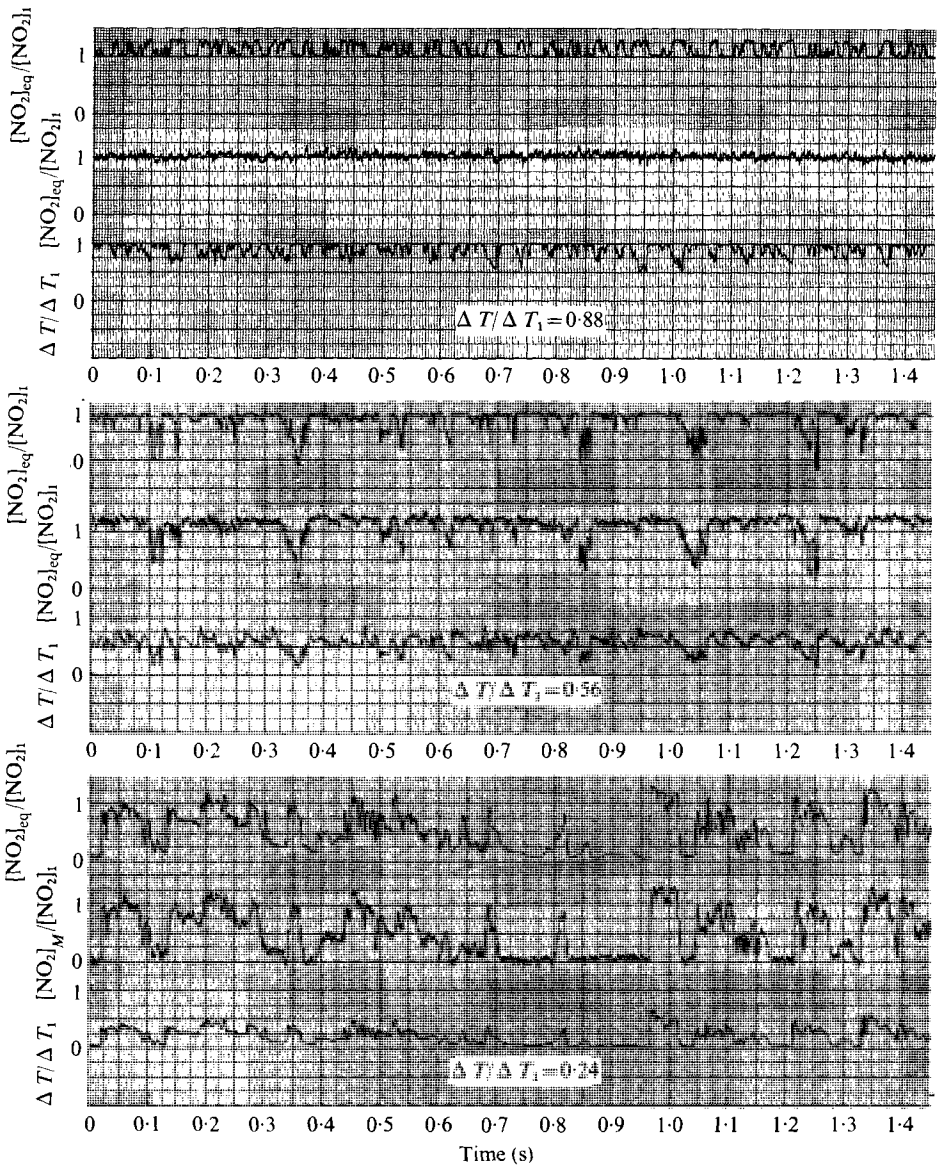

FIGURE 42. Digitized time traces for temperature/concentration data for $T_1 = 252$ °K ($u_1 = 23$ ft/s, $x - x_0 = 18{\cdot}5$ in.).

also grateful to Professors Paul Libby, Frank Champagne, Robert Bilger and Israel Wygnanski for many enlightening discussions. This research was supported by the Advanced Research Projects Agency of the Department of Defense and was monitored by Space and Missile Systems Organization, Air Force Systems Command under Contract F04701-71-C-0040. Also, I wish gratefully to acknowledge the technical support of Mr Harald Rungaldier of TRW and the continuing support and encouragement of Mr Robert Moore of ARPA. Finally, a special note of appreciation must be made to Mr Dewey Rowland of TRW for his enthusiastic support and outstanding technical assistance in carrying out the current experimental investigation.

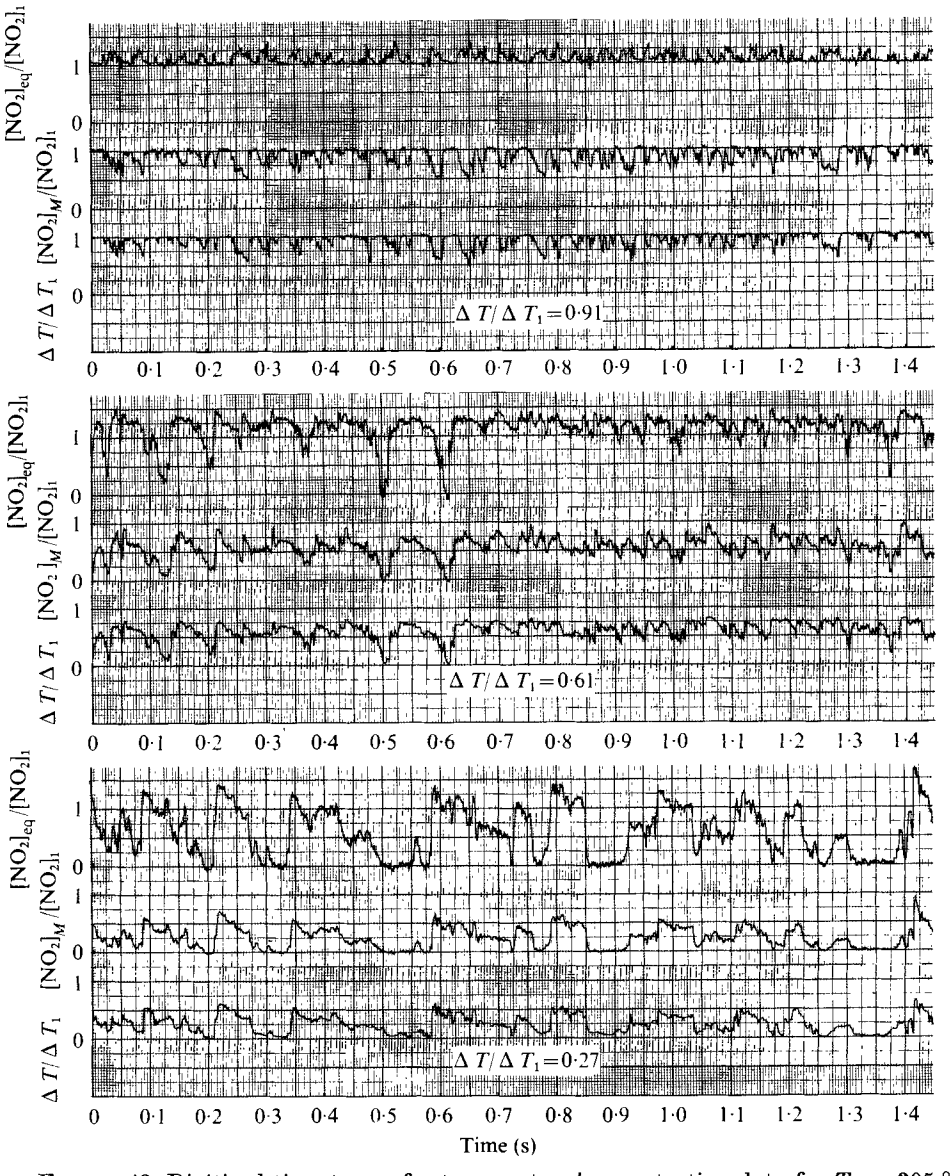

FIGURE 43. Digitized time traces for temperature/concentration data for $T_1 = 305$ °K ($u_1 = 23$ ft/s, $x - x_0 = 18{\cdot}5$ in.).

REFERENCES

ALBER, I. E. & BATT, R. G. 1976 Diffusion limited chemical reaction in a turbulent shear layer. *A.I.A.A. J.* **14**, 70–76.

BATT, R. G. 1975 Some measurements on the effect of tripping the two-dimensional shear layer. *A.I.A.A. J.* **13**, 245–246.

BATT, R. G., KUBOTA, T. & LAUFER, J. 1970 Experimental investigation of the effect of shear flow turbulence on a chemical reaction. *A.I.A.A. Paper* no. 70-271.

BECKER, H. A., HOTTEL, H. C. & WILLIAMS, G. C. 1967 The nozzle-fluid concentration field of the round, turbulent free jet. *J. Fluid Mech.* **30**, 285–303.

BILGER, R. W. 1976 The structure of diffusion flames. *Combust. Sci. Tech.* **13**, 155–170.

BOEHMAN, L. I. 1967 An investigation of momentum and mass transport properties in isoenergetic flows. *Illinois Inst. Tech. Rep.* ARL 67-0058.

BRADBURY, L. J. S. 1965 The structure of a self-preserving turbulent plane jet. *J. Fluid Mech.* **23**, 31–64.

BRADSHAW, P. 1966 The effect of initial conditions on the development of a free shear layer. *J. Fluid Mech.* **26**, 225–236.

BRADSHAW, P. 1967 Irrotational fluctuations near a turbulent boundary layer. *J. Fluid Mech.* **27**, 209–230.

BRADSHAW, P., FERRISS, D. H. & JOHNSON, R. H. 1964 Turbulence in the noise-producing region of a circular jet. *J. Fluid Mech.* **19**, 591–624.

BROWN, G. L. & ROSHKO, A. 1974 On density effects and large structure in turbulent mixing layers. *J. Fluid Mech.* **64**, 775–816.

BUSH, W. B., FELDMAN, P. S. & FENDELL, F. E. 1976 On diffusion flames in turbulent shear flows; modeling reactant consumption in a mixing layer. *Combust. Sci. Tech.* **13**, 27–55.

CASTRO, I. P. & BRADSHAW, P. 1976 The turbulence structure of a highly curved mixing layer. *J. Fluid Mech.* **73**, 265–304.

CHAMPAGNE, F. H., PAO, Y. H. & WYGNANSKI, I. J. 1976 On the two-dimensional mixing region. *J. Fluid Mech.* **74**, 209–250.

CHANDRSUDA, C., MEHTA, R. D., WEIR, A. D. & BRADSHAW, P. 1977 Effect of free-stream turbulence on large structure in turbulent mixing layers. Submitted to *J. Fluid Mech.*

CHUNG, P. M. 1969 A simplified statistical model of turbulent chemically reacting shear flows. *A.I.A.A. J.* **7**, 1982–1991.

CORRSIN, S. & UBEROI, M. S. 1949 Spectra and diffusion in a round turbulent jet. *N.A.C.A. Rep.* no. 1040.

DAVIES, P. O. A. L. 1966 Turbulence structure in free shear layers. *A.I.A.A. J.* **4**, 1971–1978.

DAVIES, P. O. A. L., FISHER, M. J. & BARRATT, M. J. 1963 The characteristics of the turbulence in the mixing region of a round jet. *J. Fluid Mech.* **15**, 337–367.

DEMETRIADES, A. 1968*a* Turbulent front structure of an axisymmetric compressible wake. *J. Fluid Mech.* **34**, 465–480.

DEMETRIADES, A. 1968*b* Turbulence measurements in an axisymmetric compressible wake. *Phys. Fluids* **11**, 1841–1852.

DIMOTAKIS, P. E. & BROWN, G. L. 1976 The mixing layer at high Reynolds number: large-structure dynamics and entrainment. *J. Fluid Mech.* **78**, 525–560.

DONALDSON, C. DUP. & VARMA, A. K. 1976 Remarks on the construction of a second-order closure description of turbulent reacting flows. *Combust. Sci. Tech.* **13**, 55–79.

FIEDLER, H. E. 1974 Transport of heat across a plane turbulent mixing layer. *Adv. in Geophys.* **18**, 93–109.

FIEDLER, H. E. 1975 On turbulent structure and mixing mechanism in free turbulent shear flows. In *Turbulent Mixing in Nonreactive and Reactive Flows. A Project Squid Workshop*, pp. 381–410. Plenum.

FORSTALL, W. & SHAPIRO, A. H. 1950 Momentum and mass transfer in coaxial gas jets. *J. Appl. Mech.* **17**, 399–408.

FORTHMANN, E. 1934 *Ing. Arch.* **5**, 42–61.

GIAUQUE, W. F. & KEMP, J. D. 1938 The entropies of nitrogen tetroxide and nitrogen dioxide. *J. Chem. Phys.* **6**, 40–52.

GIBSON, M. M. 1963 Spectra of turbulence in a round jet. *J. Fluid Mech.* **15**, 161–173.

GLASSTONE, S. 1946 *Textbook of Physical Chemistry*, 2nd edn. Van Nostrand.

GRANT, H. L. 1958 The large eddies of turbulent motion. *J. Fluid Mech.* **4**, 149–190.

HALL, T. C. & BLACET, F. E. 1952 Separation of the absorption spectra of NO_2 and N_2O_4 in the range of 2400–5000 Å. *J. Chem. Phys.* **20**, 1745–1749.

HINZE, J. O. 1959 *Turbulence*, 1st edn. McGraw-Hill.

IKAWA, H. & KUBOTA, T. 1975 Investigation of supersonic turbulent mixing layer with zero pressure gradient. *A.I.A.A. J.* **13**, 566–572.

JONES, B. G., PLANCHON, H. P. & HAMMERSLEY, R. J. 1973 Turbulent correlation measurements in a two-stream mixing layer. *A.I.A.A. J.* **11**, 1146–1150.

KOLPIN, M. A. 1964 The flow in the mixing region of a jet. *J. Fluid Mech.* **18**, 529–548.

LAWRENCE, J. C. 1956 Intensity, scale and spectra of turbulence in mixing region of free subsonic jet. *N.A.C.A. Rep.* no. 1292.

LEE, J. & BRODKEY, R. S. 1963 Light probe for the measurement of turbulent concentration fluctuations. *Rev. Sci. Instrum.* **34**, 1086–1090.

LEES, L. & HROMAS, L. 1962 Turbulent diffusion in the wake of a blunt-nosed body at hypersonic speeds. *J. Aero. Sci.* **29**, 976–993.

LIBBY, P. A. 1976 On turbulent flows with fast chemical reactions. Part III: Two dimensional mixing with highly dilute reactants. *Combust. Sci. Tech.* **13**, 79–98.

LIEPMANN, H. W. & LAUFER, J. 1947 Investigation of free turbulent mixing. *N.A.C.A. Rep.* no. 1257.

LIN, S. C. 1966 A bimodal approximation for reacting turbulent flows. I. Description of the model. II. Example of quasi-one-dimensional wake flow. *A.I.A.A. J.* **4**, 202–216.

LIN, S. C. & HAYES, J. E. 1964 A quasi-one-dimensional treatment of chemical reactions in turbulent wakes of hypersonic objects. *A.I.A.A. J.* **2**, 1214–1222.

MAYER, E. & DIVOKY, D. 1966 Correlation of intermittency with preferential transport of heat and chemical species in turbulent shear flows. *A.I.A.A. J.* **4**, 1995–2000.

MOORE, D. W. & SAFFMAN, P. G. 1975 The density of organized vortices in a turbulent mixing layer. *J. Fluid Mech.* **69**, 465–473.

NYE, J. O. & BRODKEY, R. S. 1967 Light probe for measurement of turbulent concentration fluctuations. *Rev. Sci. Instrum.* **38**, 26–28.

O'BRIEN, E. E. 1971 Turbulent mixing of two rapidly reacting chemical species. *Phys. Fluids* **14**, 1326–1331.

OH, Y. H. & BUSHNELL, D. M. 1975 Influence of external disturbances and compressibility on free turbulent mixing. Aerodynamic analysis requiring advanced computors. *N.A.S.A. Special Publ.* no. 347, pp. 341–376.

PATEL, R. P. 1973 An experimental study of a plane mixing layer. *A.I.A.A. J.* **11**, 67–71.

PHILLIPS, O. M. 1955 The irrotational motion outside a free turbulent boundary. *Proc. Camb. Phil. Soc.* **51**, 220–229.

PROUDIAN, A. P. & FELDMAN, S. 1965 A new model of mixing and fluctuations in a turbulent wake. *A.I.A.A. J.* **3**, 602–609.

RAGSDALE, R. G. & EDWARDS, O. J. 1965 Data comparisons and photographic observations of coaxial mixing of dissimilar gases at nearly equal stream velocities. *Lewis Res. Center, N.A.S.A. Tech. Note* D-3131.

ROSENSWEIG, R. E. 1959 Measurement and characterization of turbulent mixing. Ph.D. thesis, M.I.T.

ROSENSWEIG, R. E., HOTTEL, H. C. & WILLIAMS, G. C. 1961 *Chem. Engng Sci.* **15**, 111–133.

ROSHKO, A. 1976 Structure of turbulent shear flows: a new look. *A.I.A.A. J.* **14**, 1349–1357.

SPALDING, D. B. 1976 Mathematical models of turbulent flames; a review. *Combust. Sci. Tech.* **13**, 3–25.

SPENCER, B. W. & JONES, B. G. 1971 Statistical investigation of pressure and velocity fields in the turbulent two-stream mixing layer. *A.I.A.A. Paper* no. 71-813.

SUNYACH, M. 1971 Contribution à l'étude des frontières d'écoulements turbulents libres. Sc.D. thesis, Université Claude Bernard de Lyon.

SUNYACH, M. & MATHIEU, J. 1969 Mixing zone of a two-dimensional jet. *Int. J. Heat Mass Transfer* **12**, 1679–1697.

SUTTON, E. A. 1968 Chemistry in pure-air hypersonic wakes. *A.I.A.A. J.* **6**, 1873–1882.

SUTTON, G. W. & CAMAC, M. 1968 Wake-temperature turbulent fluctuation decay rates deduced from O_2 radiation. *A.I.A.A. J.* **6**, 2402–2410.

TORR, H. L. 1962 Mass transfer in dilute turbulent and non-turbulent systems with rapid irreversible reactions and equal diffusivities. *A.I.Ch.E. J.* **8**, 70–78.

TOWNSEND, A. A. 1949 Momentum and energy diffusion in the turbulent wake of a cylinder. *Proc. Roy. Soc.* A **197**, 124–140.

TOWNSEND, A. A. 1956 *The Structure of Turbulent Shear Flow*, 1st edn. Cambridge University Press.

WEBB, W. H. & HROMAS, L. A. 1965 Turbulent diffusion of a reacting wake. *A.I.A.A. J.* **3**, 826–837.

WEGENER, P. P. 1959 Supersonic nozzle flow with a reacting gas mixture. *Phys. Fluids* **2**, 264–275.

WILLS, J. A. B. 1964 On convection velocities in turbulent shear flows. *J. Fluid Mech.* **20**, 417–432.

WINANT, C. D. & BROWAND, F. R. 1974 Vortex pairing: the mechanism of turbulent mixing layer growth at moderate Reynolds number. *J. Fluid Mech.* **63**, 237–255.

WYGNANSKI, I. & FIEDLER, H. 1969 Some measurements in the self-preserving jet. *J. Fluid Mech.* **38**, 577–612.

WYGNANSKI, I. & FIEDLER, H. E. 1970 The two-dimensional mixing region. *J. Fluid Mech.* **41**, 327–361.

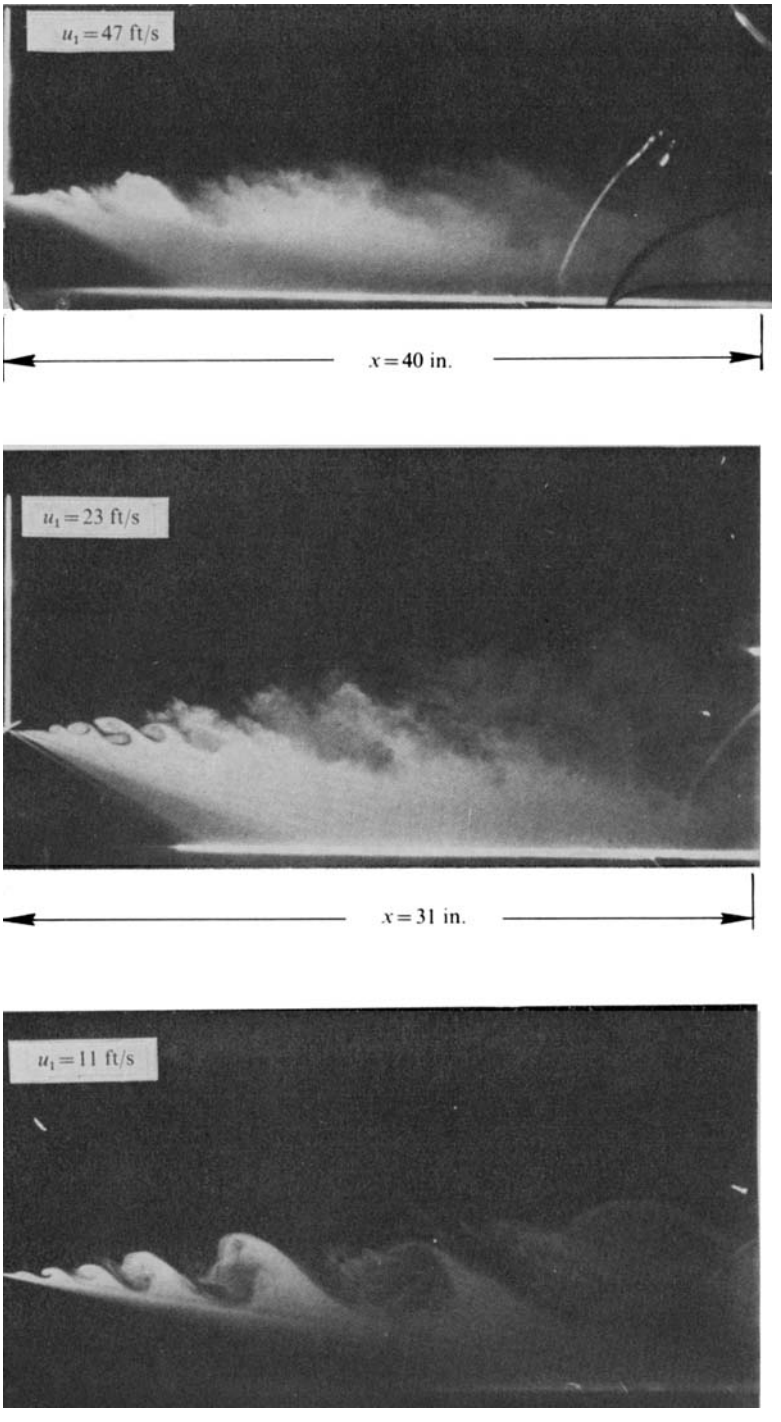

FIGURE 4. Side-scatter photographs of smoke-seeded shear layer discharging into ambient air.

FIGURE 5. Initial development of smoke-seeded turbulent shear layer at low Re (u_1 = 11 ft/s, L_{REF} = 21 in., 64 frames/s).

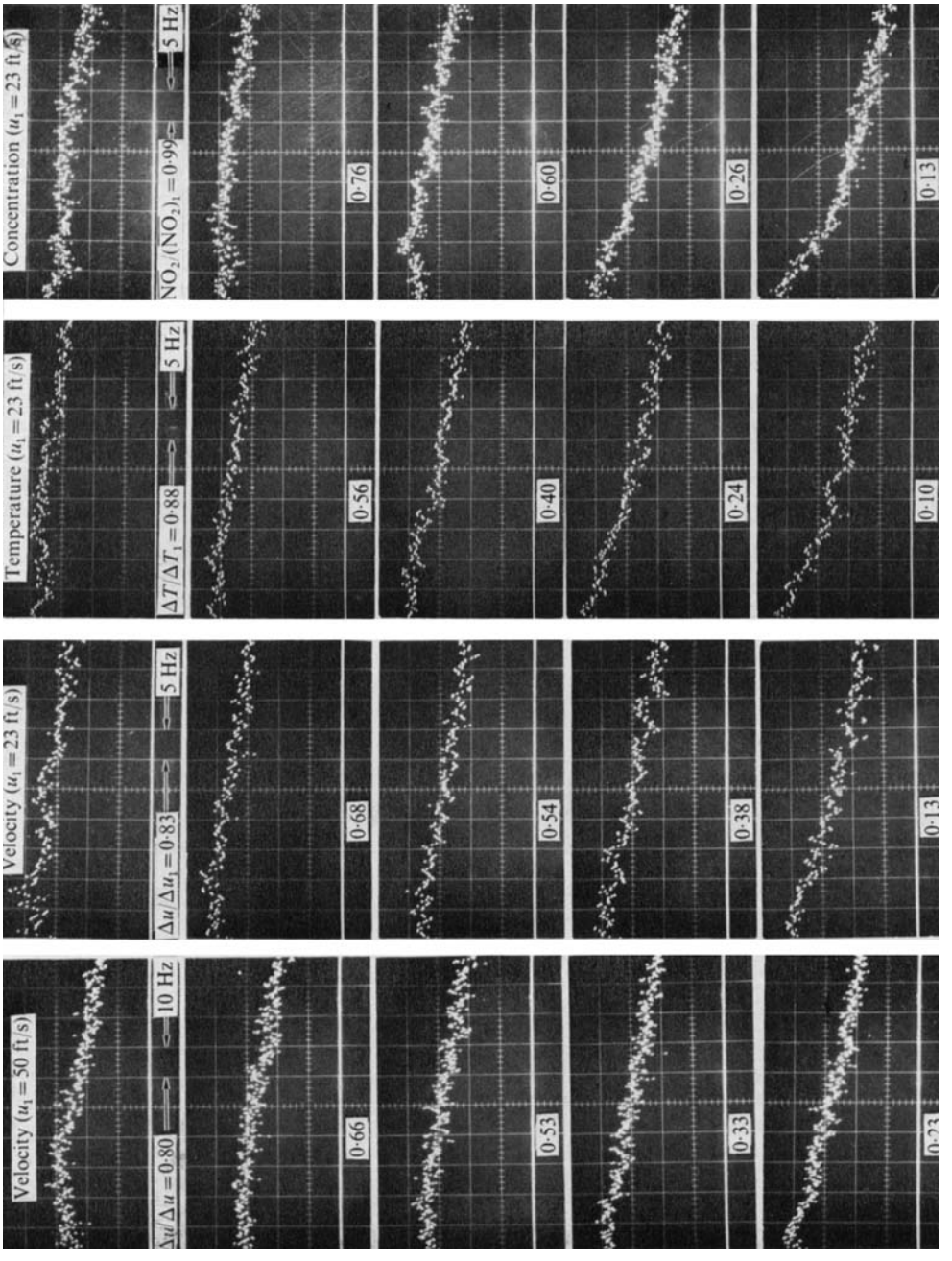

FIGURE 17. Raw spectra data (6·6 dB/cm, $x - x_0 = 18{\cdot}5$ in.).

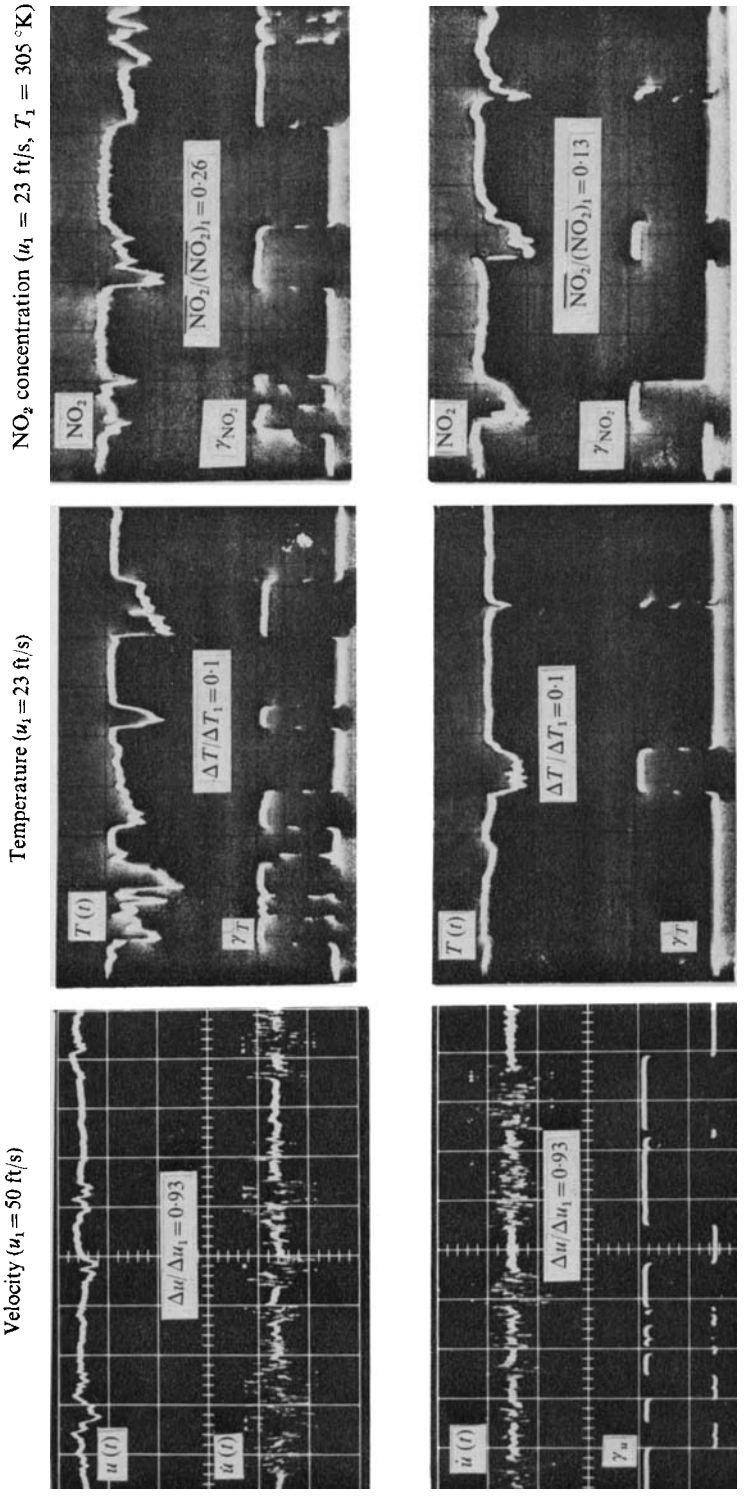

FIGURE 20. Oscilloscope traces of intermittency signals.

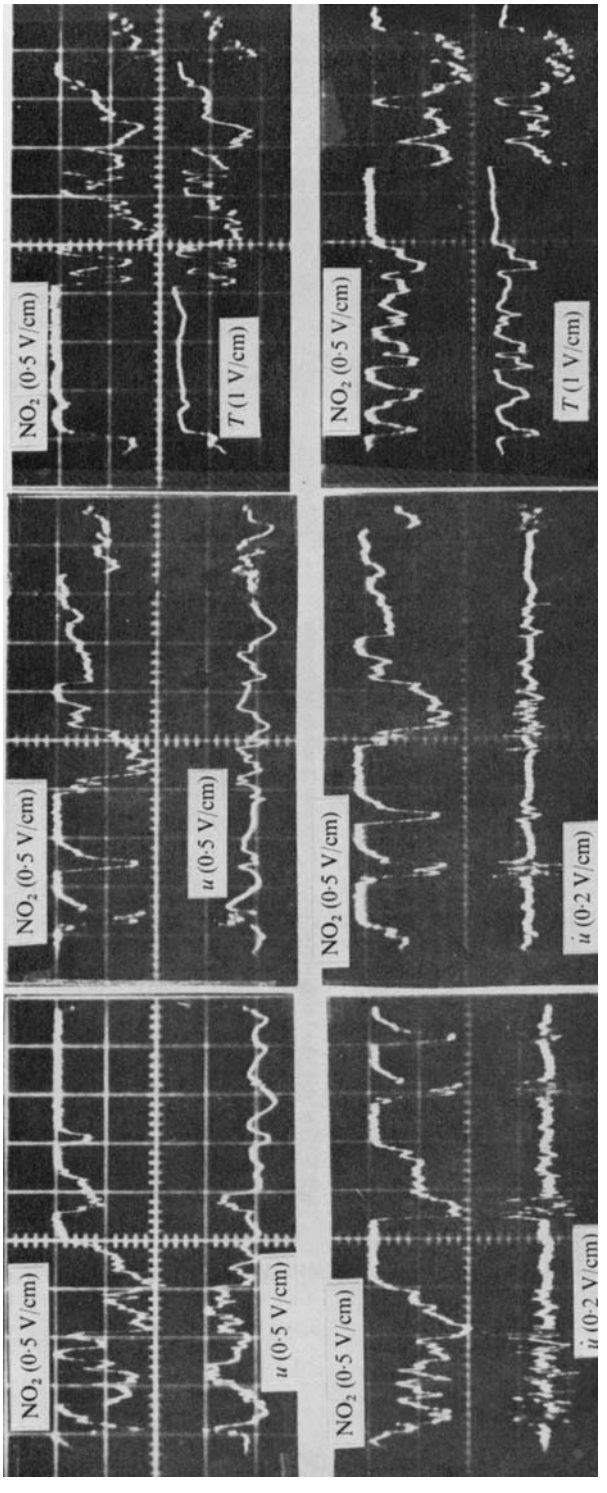

FIGURE 22. Simultaneous oscilloscope traces of velocity, temperature and concentration ($u_1 \approx 23$ ft/s, $x - x_0 = 18{\cdot}5$ in., $\Delta T/\Delta T_1 = 0{\cdot}10$, $0{\cdot}1$ s cm^{-1}).

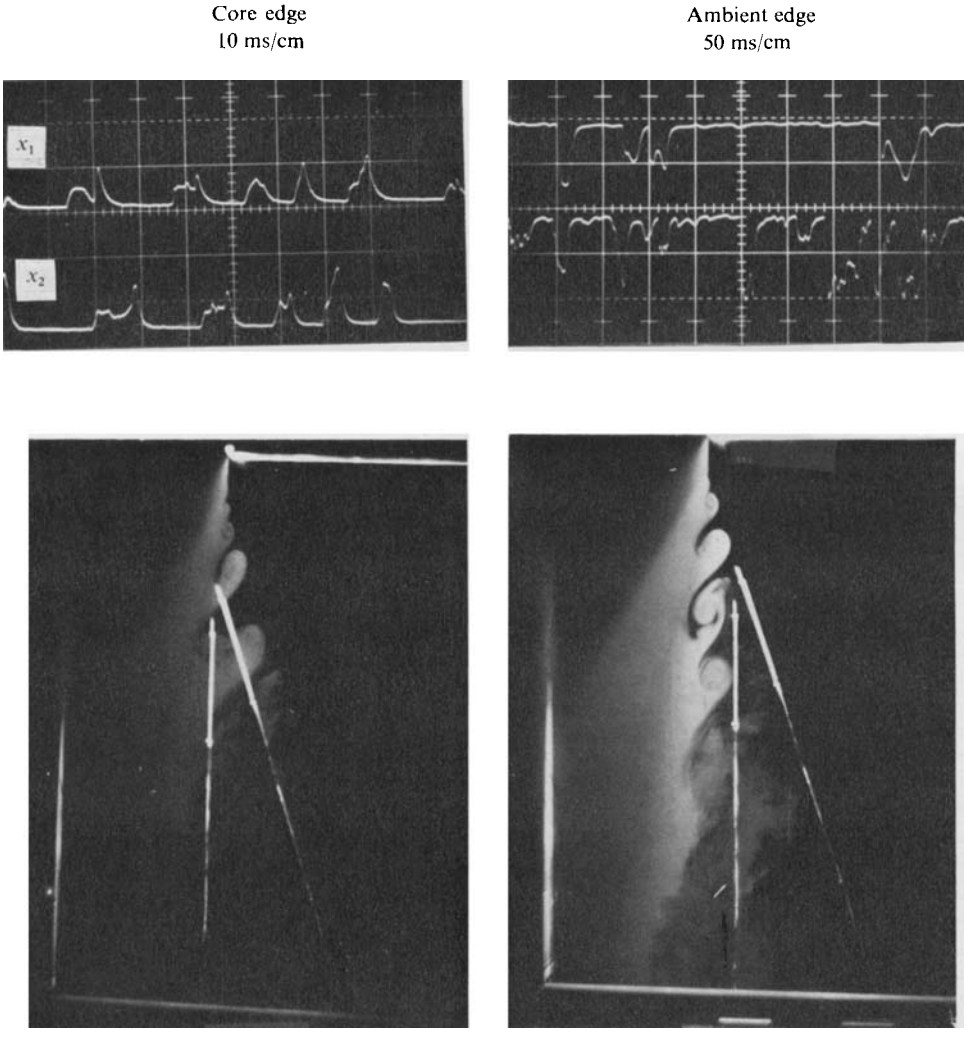

FIGURE 27 (*a*). For legend see facing page.

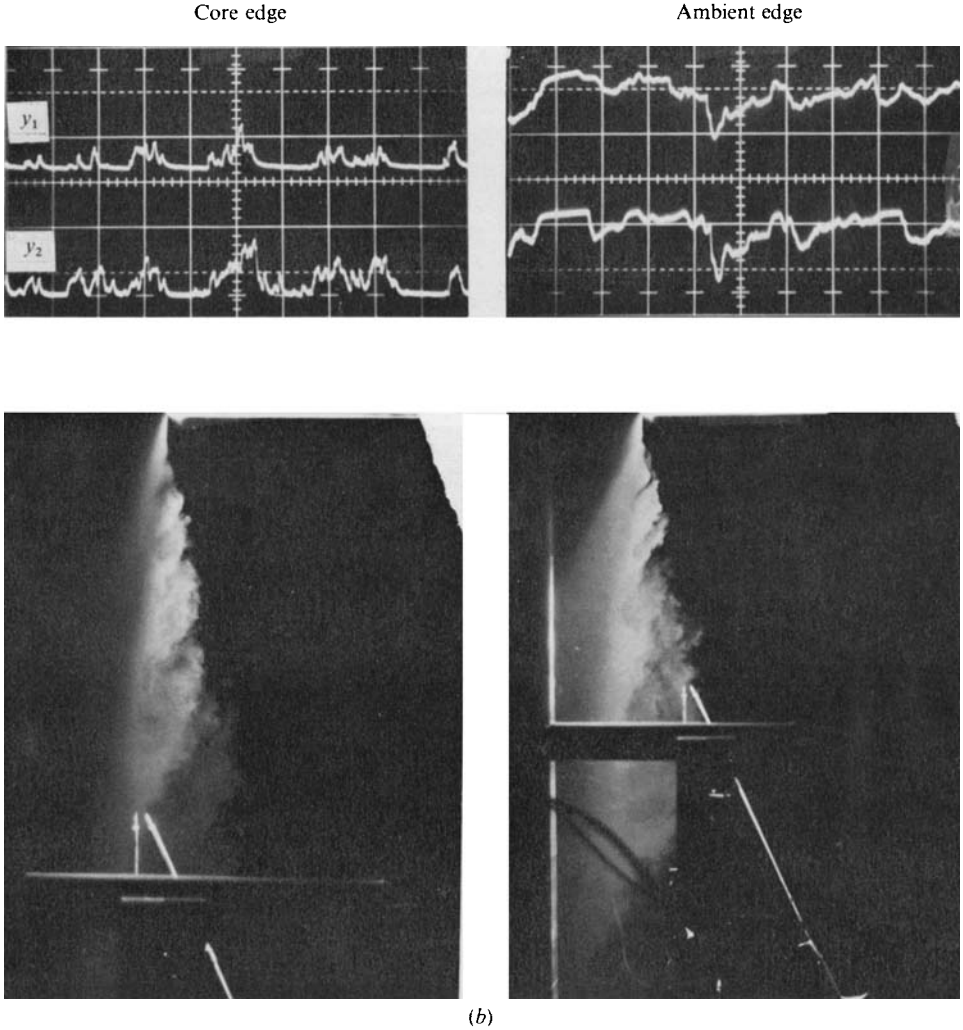

(*b*)

FIGURE 27. Temperature oscilloscope traces with simultaneous ($t = 0$) side-scatter photographs of smoke-seeded shear layer ($u_1 = 23$ ft/s, $\Delta T_1 = 5$ °C, 2·5 °C/cm). (*a*) Axial correlation measurements ($x_{top} = 4$ in., $x_2 - x_1 = 1$ in.). (*b*) Lateral correlation measurements ($x = 15$ in., $y_2 - y_1 = 0{\cdot}5$ in., 50 ms/cm).

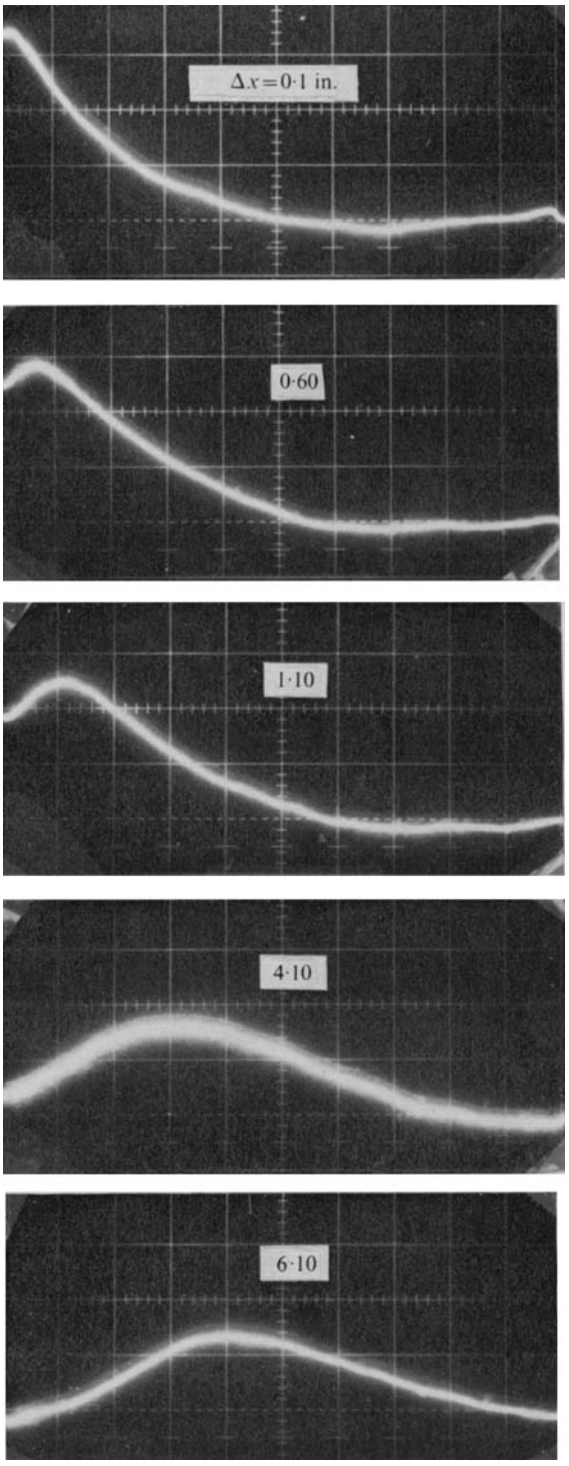

FIGURE 28. Broad-band temperature space/time correlations (u_1 = 23 ft/s. $\Delta T/\Delta T_1$ = 0·30, $x_{fix} - x_0$ = 18·5 in., 5 ms/cm).